Cold Flows in Galaxy Formation

Cold Flows in Galaxy Formation

By

Rory M. Woods, B.Sc.

A Thesis

Submitted to the School of Graduate Studies

in Partial Fulfilment of the Requirements

for the Degree

Master of Science

McMaster University

MASTER OF SCIENCE (2011) McMaster University

(Physics and Astronomy) Hamilton, Ontario

TITLE: Cold Flows in Galaxy Formation

AUTHOR: Rory Woods, B.Sc. (Mount Allison University)

SUPERVISOR: Hugh Couchman, James Wadsley

NUMBER OF PAGES: ix, 89

Abstract

We present a numerical study of gas accretion into galaxies using the SPH code, Gasoline. Numerical tests on shock treatment in Gasoline are run to evaluate how well cosmological-scale, high Mach number shocks are treated. We find that shock solutions are far too noisy, and in specific density and metallicity regimes, this seeds a phase separation instability of hot and cold gas. We propose this instability as the source of cold blobs seen in many numerical simulations. We find that improved shock behavior is primarily attained through increased viscosity parameters.

Analysis is also performed on four cosmological simulations from the McMaster Unbiased Galaxy Simulations (MUGS) (Stinson et al., 2010). In agreement with recent literature, we find cold flows of gas seeded by dark matter filaments stretching far into the inner galaxy in all analyzed galaxies. Tracking of star and gas particles is performed, and we find that cold mode accretion makes up between 40% and 60% of total gas accretion. As well, we find that cold gas is in general very quickly formed into stars, and that between 40% and 70% of total star mass comes from cold gas accretion.

Acknowledgements

First and foremost, I would like to extend a huge thank you to my two advisors, James Wadsley and Hugh Couchman. Your guidance and patience throughout this masters has been fantastic, and I appreciate all the time you've put in to helping me learn. Despite the huge cultural barriers between an Australian, a Brit, and an American, and the impossibly thick accents, we still managed to do science!

I'd also like to thank collaborators who helped make my life easier, including Greg Stinson, Tom Quinn, Eric Carlson, Sijing Shen, Sarah Nickerson, and the whole PyNBody group. In contrast, I'll offer a big "No Thanks" to that which made my life harder - IDL. Burn in a fire you crazy programming language.

To the McMaster Physics & Astronomy department - thank you. The department certainly has its act together and treats students well, and it really makes a difference throughout the degree. The efforts don't go unnoticed!

To all of my friends who helped me along the way, thank you so much. A graduate student can only take so much without the mutual misery and support of other wonderful grad students to stay sane. I'd specifically like to thank Patrick Rogers for all his help and for putting up with my constant nagging. You got a glass of scotch on me. As well, a big thanks to Mikhail Klassen for helping to lead the Python charge and for all the plotting help. Finally, to all the other defending students - thanks for taking this journey with me!

To all of my good friends elsewhere in the world - specifically Scott MacEwan, Brian Crouse, Brenna Douglas - Thanks for always being there.

Finally, to my family back in Maine - thanks for your constant support and love. It means more than anything.

Table of Contents

List of Figures

List of Tables

Chapter 1

Introduction

1.1 The Lambda Cold Dark Matter Model

Our view of The Universe has changed dramatically over the past century. Observations of galaxies in clusters (Zwicky, 1937) and of the rotation curves of galaxies (e.g. Rubin et al. (1978)) have produced velocities that are much too high to be accounted for only by visible matter. Assuming standard gravity, there must thus be a large amount of unseen mass affecting the dynamics on galaxy scales and larger, termed Dark Matter (DM). The physical origin of DM is still not well known; however comparisons of simulations and theoretical structure formation predictions with observations, e.g. of substructure (Williams et al., 1999) or the Lyman alpha forest (Crotts, 1988), suggest this matter must have negligible initial random motion in order to form structure in the right format (hierarchically; see section 1.2) and on the right time scales. We thus call the mass Cold Dark Matter (CDM).

Observations by Edwin Hubble (Hubble, 1929) showed that the farther away a galaxy is from our own, the faster it appears to be receding. This was some of the first evidence that our Universe was not static, but was in fact expanding. It wasn't until many years later, however, with observations of distant type 1a Supernovae (SNe) that the nature of this expansion was understood (Riess et al., 1998; Perlmutter et al., 1999). The observations of type 1a SNe suggest that not only is our universe expanding, but it is currently doing so at an accelerating rate.

The expansion of our Universe can be described by solving Einstein's field equations for a particular Universe. If we assume an isotropic, homogenous Universe, the general solution is Friedmann's equation (e.g. Peebles (1993)),

$$\dot{R}^2 - \frac{8}{3}\pi G\rho R^2 - \frac{1}{3}\Lambda c^2 R^2 = -kc^2. \tag{1.1}$$

Here, R is the scale factor of the Universe, ρ is the density (including contributions from matter and radiation), and k is a value of either -1, 0, or 1, that describes the curvature of the Universe. The Λ term was not originally present in Friedmann's equation. Historically, Λ was a constant added by Einstein to his field equations to balance out gravity in order to provide a static Universe. However, Λ also allows for an accelerating Universe and is thus included. Our current standard cosmology, including the cosmological constant Λ and CDM, is not surprisingly called the Lambda Cold Dark Matter (ΛCDM) cosmology. Since the physical origin of the Λ term is not yet understood, it is often referred to as "dark energy" or "vacuum energy". Note, however, that a cosmological constant, Λ, is just one possibility for dark energy.

Observations suggest that k is consistent with 0, or a "flat Universe". Setting k to zero in equation 1.1 gives a familiar Euclidean-like equation of energy conservation. If we then solve for density, we can define what is called the critical density (ρ_c) of the Universe. Above this value, the universe has a closed space-time metric; below this value, and open metric. Solving equation 1.1 yields

$$\rho_c = \frac{3H^2}{8\pi G}, \tag{1.2}$$

with H being the ratio of the time derivative of the scale factor to the scale factor, $\dot{R}/R$. Most papers express the density of the Universe as a ratio to the critical density, $\Omega = \rho/\rho_c$. In general, the term is also broken into separate contributions from each component of the universe; The current best estimates are given in the Wilkinson Microwave Anisotropy Probe (WMAP) seven year results (Komatsu et al., 2011)

$$\begin{aligned}
\Omega_\Lambda &= 0.725 \pm 0.016, \\
\Omega_b &= 0.0458 \pm 0.0016, \\
\Omega_{DM} &= 0.229 \pm 0.015, \\
H_0 &= 70.2 \pm 1.4 \text{km } s^{-1}
\end{aligned}$$

where Ω_Λ is the vacuum or dark energy-density, b is baryonic matter, and DM is dark matter. These values imply that visible matter only makes up about five percent of the total energy-density in our Universe, and only about seventeen percent of matter in the Universe. It is for this reason that the dynamics and evolution of our Universe is largely determined by dark energy and dark matter, with the dynamics of galaxies mainly determined by dark matter.

1.2 Hierarchical Structure Formation

One of the predictions of a ΛCDM cosmology is that smaller scales are the first to enter the non-linear regime. This means that merging of smaller structures occurs in order to form larger structures in the Universe. This is called a "bottom-up" or hierarchical structure formation (e.g. Peebles (1978)).

Initial perturbations in the DM, assumed to be Gaussian, cause certain regions to undergo gravitational collapse into Jean's mass halos. Since DM can not cool via radiation, but baryonic matter can, most of the baryonic matter collapsed down into the centers of these potential wells. These were some of the earliest visible objects in the Universe. From here, larger structures began forming through merging of these small halos.

A merger between two galaxies provides a number of very interesting dynamical effects. Even just close passages of bodies can cause thickening and heating of the galactic disk. Full on collisions and mergers can also cause tilting and warping of the disk, induced bars and spiral perturbations, or in extreme cases, can totally destroy the disk. In any case, a merger is usually fairly easy to identify due to the visible dynamical effects (See e.g. Sanchez-Saavedra et al. (1990); Nelson & Tremaine (1995); Velazquez & White (1999); Velazquez (2001); Tsuchiya (2003); Kazantzidis et al. (2008, 2009)).

In cases where the merging galaxies are rich in gas, the merger usually triggers huge bursts of star formation. The rate at which stars are forming in such galaxies is generally high enough that it would deplete the gas reservoir in a very short period of time. Up until recently, it was thought that mergers were associated with all strong star formation seen in galaxies. However, there exist many starburst galaxies at high redshifts without signs of a merger (Chapman et al., 2004; Förster Schreiber et al., 2006; Genzel et al., 2006, 2008; Stark et al., 2008), suggesting that other mechanisms may be responsible for starbursts.

In order to maintain such high SFRs, gas must be delivered to the galaxy at a similar rate. However, in order to preserve a disk, there are strict limits on the amount of gas that can be deposited into a disk via mergers (Toth & Ostriker, 1992). This has led many authors to begin to revise the classical view of gas accretion.

1.3 Fueling Galaxies: Gas Accretion

The traditional view of galaxy formation stems from a number of early theoretical papers (Rees & Ostriker, 1977; Silk, 1977; Fall & Efstathiou, 1980). These authors paint a fairly simple first analysis of galaxy formation which suggests that spherically infalling gas shock heats to the virial temperature, creating a thermally supported halo of gas. In the inner regions of the halo, gas is able to effectively radiate away much of its thermal energy, enabling the gas to cool and collapse down to a centrifugally supported disk.

Many of the galaxy formation semi-analytic models (SAMs) adopt this view (White & Frenk, 1991; Kauffmann et al., 1993; Cole et al., 1994; Avila-

Reese et al., 1998; Mo et al., 1998; Somerville & Primack, 1999; Stringer & Benson, 2007; Kampakoglou & Silk, 2007), where a density profile is used and a cooling radius is then calculated, specifying the point at which gas is able to collapse down.

Over the last decade, a number of authors have argued that not all accreting gas will necessarily shock. In order for gas to shock, the compression rate of the infalling gas must be larger than the cooling rate (Dekel & Birnboim, 2006). This means that smaller halos, which have smaller dynamical times, may not be able to support a shock at all as most of the compression energy would be radiated away too fast.

Most galaxies live at the nodes of the filamentary structure of DM in our Universe (Bond et al., 1996). Many authors have noted that this enables gas to effectively be funneled into the galaxy along the DM filaments (Katz et al., 1993; Katz & White, 1993; Katz et al., 1994; Bertschinger & Jain, 1994; Bond et al., 1996; Shen et al., 2006; Harford et al., 2008). It has only been in the past decade that simulations have shown that these filaments may also be a means for gas to get into a galaxy without shock heating (Birnboim & Dekel, 2003; Kereš et al., 2005; Dekel & Birnboim, 2006; Kereš et al., 2009; Ocvirk et al., 2008; Dekel et al., 2009; Brooks et al., 2009; Stewart et al., 2011). Gas that is able to accrete without shock heating is generally referred to as “cold-mode accretion,” while gas that accretes along the filaments is called a “cold flow” (a type of cold-mode accretion) (Kereš et al., 2005).

Recent papers have suggested that signatures of cold mode accretion, and specifically of cold flows, should be visible in absorption studies of galaxies, especially for MgII (Stewart et al., 2011; Kimm et al., 2011), which is optically thick in neutral hydrogen (Rigby et al., 2002), the primary component of cold mode gas. As well, it has been suggested that cold flow gas has very high specific angular momentum, and should be visible as a radial velocity offset, distinct from outflowing gas (Stewart et al., 2011). However, observational evidence for cold flows in galaxies is limited so far (e.g. Steidel et al. (2010)). For all but the closest galaxies, resolving cold flow features is very difficult due to a low covering fraction of the flows on the galaxy (Putman et al., 2009; Faucher-Giguère & Kereš, 2011). While it is possible that observations of cold-mode accretion have already been made (Stewart et al., 2011), there has yet to be a clear cut observation. For this reason, further characterizing and understanding cold-mode accretion is a very important aspect of getting a better picture of galaxy formation.

1.4 Thesis Overview

The results presented in this thesis focus on three topics. Chapter 2 will discuss the methods used to test shock treatment in the tree-SPH code, GASOLINE, and present the results of that testing. Chapter 3 will introduce the simulated galaxies that have been analyzed for cold flow characteristics and shock performance as well as talk about how the analysis was performed. The results of the analysis and the implications for computational and observational galaxy formation will also be discussed. Finally, concluding remarks are given in chapter 4.

Chapter 2

Methods

In this chapter, we present an introduction to the numerical methods, specifically Smoothed Particle Hydrodynamics (SPH), used to simulate galaxies. This includes some of the specific subgrid methods of the SPH code, Gasoline. As well, we introduce the tests used to assess our SPH code and the results of those tests.

2.1 Smoothed Particle Hydrodynamics

Smoothed Particle Hydrodynamics (SPH) is a numerical method for solving Euler's equations that was developed in 1977 as a numerical approach to non-axisymmetric problems (Gingold & Monaghan, 1977; Lucy, 1977). It turned out the method gave robust results and was fairly easily extended to include many other types of physics, and so has caught on as one of the leading computational methods in astrophysics.

SPH is a Lagrangian method; it uses particles in a co-moving reference frame that follow fluid flow. Since there will always be a discrete number of particles, some sort of smoothing is needed to approximate the continuous fluid the particles are meant to represent. This is supplied by a weighting or smoothing kernel, W_{ab}.

The kernel acts between pairs of particles in order to create a smooth approximation of physical quantities over some characteristic length, h. The kernel must be normalized in order to conserve quantities,

$$\int_0^\infty W(|\mathbf{r}-\mathbf{r}'|,h)d\mathbf{r} = 1, \tag{2.1}$$

and must also give the discrete value back in the limit of smoothing over 0 length (that is, in the limit that h goes to zero),

$$\lim_{h\to 0} W(|\mathbf{r}-\mathbf{r}'|,h) = \delta(\mathbf{r}-\mathbf{r}'), \tag{2.2}$$

where δ is the Dirac-Delta function (Monaghan, 1992). This allows calculation of some quantity A using

$$A(\mathbf{r}) = \int A(\mathbf{r}')W(|\mathbf{r}-\mathbf{r}'|,h)d\mathbf{r}'. \tag{2.3}$$

The equation can be discretized by replacing the integral with a summation and the mass element ρdV with the particle mass,

$$A(\mathbf{r}) \approx \sum_{b=1}^{N} m_b \frac{A_b}{\rho_b} W(|\mathbf{r}-\mathbf{r}'|,h)d\mathbf{r}', \tag{2.4}$$

where the subscript b refers to the quantity calculated at the position of particle b, and N is the number of neighboring particles to sum over (this is typically set between 32 and 64 for best results).

An immediate benefit of this formalism is that spatial derivatives of a quantity can be expressed easily since W is the only explicit function of position. Using this property, the derivative of a quantity can be expressed as

$$\nabla A(\mathbf{r}) \approx \sum_{b=1}^{N} m_i \frac{A_b}{\rho_b} \nabla W(|\mathbf{r}-\mathbf{r}'|, h) d\mathbf{r}'. \tag{2.5}$$

This allows momentum and energy conservation from the Euler equations to be written as

$$\frac{d\mathbf{v}_a}{dt} = -\sum_b m_b \left(\frac{P_b}{\rho_b^2} + \frac{P_a}{\rho_a^2} \right) \nabla_a W_{ab}, \tag{2.6}$$

$$\frac{du_a}{dt} = \left(\frac{P_a}{\rho_a^2} \right) \sum_b m_b \mathbf{v_b} \cdot \nabla_{\mathbf{a}} W_{ab}. \tag{2.7}$$

The above formulation lays the foundation of SPH. Many variations in the method now exist to suit a huge range of computational needs, ranging from modeling in geophysics, atmospheric science, and engineering to different fields within astrophysics, ranging from structure growth on a cosmological scale to the collision of protoplanets (Springel, 2010). As well, treatment of unresolved physics can be added at the particle level in SPH, further improving treatment of physical phenomena. The specific variations to SPH and sub-resolution physics used in Gasoline are discussed in the following section.

2.2 Gasoline

Gasoline is a parallel k-D Tree SPH code. At the base of Gasoline is the gravity solver, pkdgrav (Stadel, 2001). The gravity solver uses a modified k-

D (k-dimensional) tree in which the mass moments in each cell are represented using a fourth order multipole moment. The tree approach makes use of the fact that the details of a mass distribution are less important at further distances from a particle. Thus, contributions to the gravitational force on a particle can be approximated using the center of mass of a tree cell rather than using each separate particle within that cell. Using a tree is inherently $\mathcal{O}(n \log n)$ and provides an efficient structure for neighbor finding (Barnes & Hut, 1986), so the same gravity tree can be used for the SPH method in the hydrodynamics calculations.

Outside of normal hydrodynamics calculations (section 2.1), GASOLINE also includes subgrid methods (methods that approximate physics below the resolution limit) for star formation, SNe and stellar wind feedback, (Stinson et al., 2006), metal and thermal energy mixing (Wadsley et al., 2008), and radiative cooling due to metals (Shen et al., 2010).

2.2.1 Subgrid Physics

Star formation in GASOLINE has been implemented by Stinson et al. (2006). Gas particles are probabilistically formed into stars once they have passed density, temperature, converging flow ($\nabla \cdot \mathbf{v} < 0$), and Jeans instability criteria. The efficiency/probability of formation is a user set parameter, though the star formation efficiency is usually set at five percent, a value determined to match the Kennicut-Schmidt law (Kennicutt, 1998). Feedback from SNe is approximated using a blastwave model (McKee & Ostriker, 1977), in which a fraction of the energy from a number of type Ia and type II SNe is dumped into surrounding gas particles. The number of SNe is calculated based off of the initial mass function (IMF) of the star particle (which represents a cluster of stars) using the minimum and maximum mass generated in the star cluster. Gasoline typically uses the IMF from Kroupa et al. (1993). In order to avoid over-cooling in these dense regions, cooling is turned off for the duration of the "blastwave." SNe feedback, as well as stellar feedback from the star particles, also return both mass and metals to surrounding gas particles.

GASOLINE has recently had metal cooling implemented (Shen et al., 2010). Cooling is broken into two separate components,

$$\Lambda = \Lambda_{\mathrm{H,He}} + \Lambda_{\mathrm{metal}} \tag{2.8}$$

where $\Lambda_{\mathrm{H,He}}$ is the cooling rates due to H, H^+, He, He^+, and He^{++} and Λ_{metal} is the rate due to metals. Primordial cooling and heating is calculated from ionization rates from Abel et al. (1997). Cooling and heating rates due to metals with a UV field were calculated using the photoionization code, CLOUDY (version 07.02 Ferland et al. (1998)). To calculate rates, Shen et al. assumed a uniform UV background, also obtained from CLOUDY. The UV field is off until z = 8.9, at which point it is turned on and then evolves until z = 0. This same field is used in calculations of the primordial cooling and heating rates.

For performance, the cooling rates were stored in a look-up-table as a function of temperature, number density of particles, and redshift. Prior analysis showed that metal cooling varied linearly with metallicity, so the look up table was tabulated for solar metallicity, and results were then scaled by $Z/Z_{\odot}$,

$$\Lambda_{\text{metal}}(T, \rho, z, Z) = \frac{Z}{Z_\odot}\Lambda_{\text{metal},\odot}(T, \rho, z). \tag{2.9}$$

Further details on the cooling can be found in Shen et al. (2010), section 2.1. Diffusion is also available in GASOLINE. However, simulations used for this thesis did not include diffusion and thus it is not introduced here.

2.2.2 Shocks & Artificial Viscosity

In order to study gas accretion in galaxies, numerical solvers must be able to handle shocks in an accurate manner. Shock fronts are particularly difficult to simulate because they involve large changes in properties over very small scales: they are essentially discontinuous. In SPH, the continuous equations have become discretized (equation 2.4). Doing so makes the assumption that properties are smoothly varying on the smallest scales the numerical scheme can resolve (the smoothing length, h). In the case of shocks, where this is not a good assumption, the numerical scheme produces unphysical widening and post-shock oscillation in particle properties.

In order to improve shock behavior, many codes add artificial viscosity. The viscosity modifies the Euler equations, equations 2.6-2.7, to include an extra term,

$$\frac{d\mathbf{v}_a}{dt} = -\sum_b m_b \left(\frac{P_b}{\rho_b^2} + \frac{P_a}{\rho_a^2} + \Pi_{ab}\right) \nabla_a W_{ab}, \tag{2.10}$$

$$\frac{du_a}{dt} = \frac{1}{2}\sum_b m_b \left(\frac{P_b}{\rho_b^2} + \frac{P_a}{\rho_a^2} + \Pi_{ab}\right) \mathbf{v_{ab}} \cdot \nabla_{\mathbf{a}} W_{ab}, \tag{2.11}$$

where a or b represents the quantity evaluated at the location of particle a or b, P is pressure, ρ is density, and $\mathbf{v_{ab}}$ is the velocity between particle a and b. Note that the energy equation has been written in a different form from equation 2.7 to keep energy conservation (Evrard, 1988). As well, Galilean invariance (independence of the absolute magnitude of velocity) is preserved in equations 2.11 - 2.13 by use of $\mathbf{v}_{ab}$ rather than v_b. Codes commonly adopt the definition of Π_{ab} from Monaghan (1992),

$$\Pi_{ab} = \begin{cases} \frac{-\alpha \bar{c}_{ab} \mu_{ab} + \beta \mu_{ab}^2}{\bar{\rho}_{ab}} & \mathbf{v}_{ab} \cdot \mathbf{r}_{ab} < 0 \\ 0 & \mathbf{v}_{ab} \cdot \mathbf{r}_{ab} > 0 \end{cases}, \tag{2.12}$$

with

$$\mu_{ab} = \frac{h \mathbf{v}_{ab} \cdot \mathbf{r}_{ab}}{\mathbf{r}_{ab}^2 + \eta^2}. \tag{2.13}$$

Here, $\bar{c}_{ab}$ is the average sound speed between the two particles, $\bar{\rho}_{ab}$ is the average density, and α and β are constants, generally chosen to be 1 and 2, respectively (Monaghan & Lattanzio, 1985). It is important to note that numerical schemes should avoid introducing too much viscosity where it is not necessary. While the viscosity does help to produce ordered fluid flow and keep the code stable, excessive viscosity can produce inaccurate behavior of the fluid, such as pre-shocking or angular momentum transport. This is partially taken care of in equation 2.12 by only allowing viscosity in regions where $\mathbf{v}_{ab} \cdot \mathbf{r}_{ab} < 0$; that is, where compression is happening. However, due to the noisy nature of SPH particles, the viscosity frequently ends up acting in regions it should not.

In order to combat excessive viscosity, many codes have also adopted an explicit viscosity switch meant to reduce the contribution from artificial viscosity in regions outside of pure compression. Typically, codes have adopted the switch from Balsara (1995), particularly when shear flows are involved in a simulation,

$$S_a = \frac{|\nabla \cdot \mathbf{v}|_a}{|\nabla \cdot \mathbf{v}|_a + |\nabla \times \mathbf{v}|_a}. \tag{2.14}$$

The switch varies from 0 in regions of high rotation to 1 in regions of high compression. While the switch does help, it is still quite noisy, again due to particle noise. Even so, GASOLINE shows sufficiently good behavior in weak shock tests using the above additions to SPH (Wadsley et al., 2004).

Unfortunately, most of the testing to date does not recreate conditions similar to accretion of gas in galaxies; the tested shocks are far too weak. Gas inflow into galaxies can range from subsonic to extremely supersonic (Mach numbers on the order of 10 to 100). Code testing in this regime of shocks is thus still needed to confirm reasonable behavior.

2.3 Gasoline Testing

In order to test GASOLINE'S ability to properly deal with shocks, two test problems were set up. A "colliding flows" initial condition (IC) was tested in which a self-similar "tube" was initialized with opposing flows of gas from each end, and a spherical collapse of a gas cloud was tested, in which a cold cloud of gas with a density peak at the center is allowed to collapse under gravity.

Both tests were initially run without any subgrid physics, and the colliding flows IC was run without gravity. Follow up colliding flows tests were done with cooling (including metal cooling) turned on. All tests used 50 neighbors for SPH calculations.

2.3.1 Colliding Flows Tests

In the colliding flows test, opposing flows immediately run into each other and a shock front propagates outward. The test should roughly simulate gas accretion at the edge of the hot halo of a galaxy. For this reason, the tube was set up with similar properties to such accretion. The tube was set to have a length:width:height ratio of 16:1:1. We chose the length to be 300 kpc, similar to scales of gas accretion for galaxies. Initial velocities were set at 21.42 km/s for Mach 1 testing and 214.2 km/s for Mach 10 testing. Infall velocities of gas are typically in this range, depending on the size of the host galaxy. The temperature was set at 20,000 K for all particles. The density was set at 4×10^{-26} g cm^{-3}. Note that because the initial testing was done with an adiabatic gas model, the above scales are unimportant to the solution. The scales only become important once cooling is turned on (see table 2.2).

Initially all particles were started with $v_y = v_z = 0$. For particles with $x < 0$, velocity was set positive at one of the values specified above. For particles with $x > 0$, velocity was set negative, giving two opposing flows. However, due to the discontinuity at $x = 0$, strange behavior occurred post-shock just around $x = 0$ for the Mach 10 case. In order to improve this, the particle velocities were smoothed over a small range about $x = 0$ using the Fermi-Dirac distribution, shifted and scaled to match the two flows,

$$v(x) = \frac{2v}{e^{(x/k)} + 1} - v \qquad \text{for} - 5 < x < 5, \tag{2.15}$$

where v is the absolute value of the velocity (214.2 km/s for Mach 10) and k is a constant that determines how wide the smoothing is, chosen here to be 1.5 kpc. The resulting Mach 10 initial condition is shown in figure 2.1. Note that the smoothing was not needed for the Mach 1 tests, and that the smoothing had no effect on results beyond a few kpc of the origin.

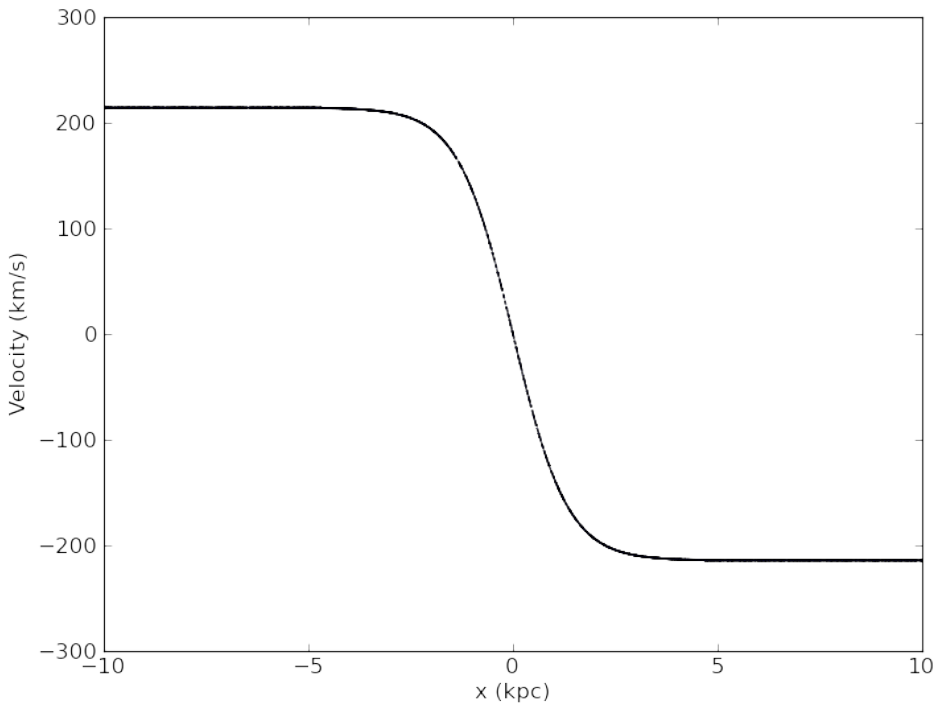

Figure 2.1: A zoomed in view of the Mach 10 colliding flow IC. Smoothing has been applied for $-5 < x < 5$. Note that all particles outside of this zoom have $v_x = \pm$ 214.2 km/s.

In order to get an idea of what numerical parameters in gasoline had the largest effect on results, the same initial condition was run while varying many different parameters. A summary of the varied parameters is presented in table 2.1. α and β are the parameters presented in equation 2.12. For any particle, the time step is calculated based off of the acceleration. This time step is then scaled up or down for higher or lower accuracy using η. η_{Courant} is a time step stability criterion that ensures the time step is small enough such that information cannot be propagated faster than the sound speed of the gas.

$\eta_{\dot{U}}$ puts a limit on the time step such that the internal energy of a particle cannot change by more than the specified value. SPH single stepping turns off variable time steps for particles and forces all particles to the lowest globally calculated time step. The viscosity limiter specifies which switch is used in equation 2.14. A value of 1 specifies that the code uses Equation 2.14, and a value of 2 specifies the use of Equation 2.20, discussed in Section 2.3.2.

Table 2.1: A list of GASOLINE parameters that were varied.

Parameter Name	**Std. Value**	**Description**
α	1	Linear velocity coefficient from eq. 2.12
β	2	Quadratic velocity coefficient from eq. 2.12
η	0.175	Acceleration time step prefactor
η_{Courant}	0.4	Courant time step prefactor
$\eta_{\dot{U}}$	0.2	Maximum % internal energy can change by in 1 step
SPH Single Stepping	0	Forces all particles to shortest time step if set to 1
Viscosity Limiter	1	Determines switch to be used in eq. 2.14. 1 is “Balsara”, 2 is “Wadsley.”

Follow up shock tests were run in which the cooling and a UV field had been turned on. For these tests, only the parameter that was found to be the most important from initial testing, α, was varied. Initial conditions were set such that the metallicity of all particles was set to 0.01 solar metallicity (0.01 $Z_\odot$), approximately that of the intergalactic medium (IGM) (Shen et al., 2010). The density of the flows was varied to try to accurately reproduce different regimes of gas flow in galactic systems. All runs otherwise had the same properties as the non-cooling runs. A summary of the cooling runs is provided in table 2.2.

Table 2.2: A summary of the cooled colliding flows that were run. All tests had a metallicity of 0.01 $Z_\odot$ and a constant UV field.

Run	**Density**	
	(g cm^{-3})	(atoms cm^{-3})
d1	4×10^{-29}	2.5×10^{-5}
d2	4×10^{-28}	2.5×10^{-4}
d3	4×10^{-27}	2.5×10^{-3}
d4	4×10^{-26}	2.5×10^{-2}

The average density of the universe can be calculated by using measured values of Ω and the definition of ρ_{crit}, as well as the fact that density scales as (1+z)^3,

$$\bar{\rho_b}(z) = \Omega_b \rho_{crit}(1+z)^3. \tag{2.16}$$

For a WMAP7 cosmology, we have that $\bar{\rho_b}(z) \approx 4.2 \times 10^{-7}(1+z)^3$ atoms cm^{-3}. If we use the traditional overdensity of 178 at the virial radius (Peebles, 1976), we can also get the average density at the edge of the hot halo. This gives an approximate range of 1×10^{-7} to 1×10^{-2} atoms cm^{-3} depending on proximity to the galaxy and redshift. Thus, d1-d2 approximately represent gas shocking at the edge of the hot halo and d3-d4 approximately represent gas shocking in cold flows within the hot halo or at the edge of the disk. These values are also similar density values to those used in Shen (2010) for comparison with cooling functions.

2.3.2 Colliding Flows Results

The solutions for two colliding flows approach a mathematical limit as the Mach number of one of the flows becomes hypersonic with respect to the other,

$$\frac{P_2}{P_1} = \frac{2\gamma}{\gamma+1} M_1^2, \tag{2.17}$$

$$\frac{\rho_2}{\rho_1} = \frac{\gamma+1}{\gamma-1}, \tag{2.18}$$

$$\frac{T_2}{T_1} = \frac{(2\gamma)(\gamma+1)^2}{\gamma+1} M_1^2, \tag{2.19}$$

where 1 and 2 denote each flow, P is pressure, ρ is density, T is temperature, M is Mach number, and γ is the heat capacity ratio. This problem, in which we have two sections of gas with constant properties and a discontinuity in between, is called a "Riemann Problem." Our test flows have been set up with $\gamma = 5/3$ and a Mach number of 10. Upon initial collision, a shock wave propagates outward at approximately 73 km/s. Thus, the actual Mach number of the shock wave is approximately 13.4. In all plots, the solution to the Riemann problem has been shown with a red line and each particle is plotted as a black point. All plots are shown at step 80, which corresponds to 377 Myrs after the collision. Using a slightly later time allows us to observe how the shock evolves over time in a single snap shot since the simulation is self similar, and thus the x distance of the shock is a direct proxy for time.

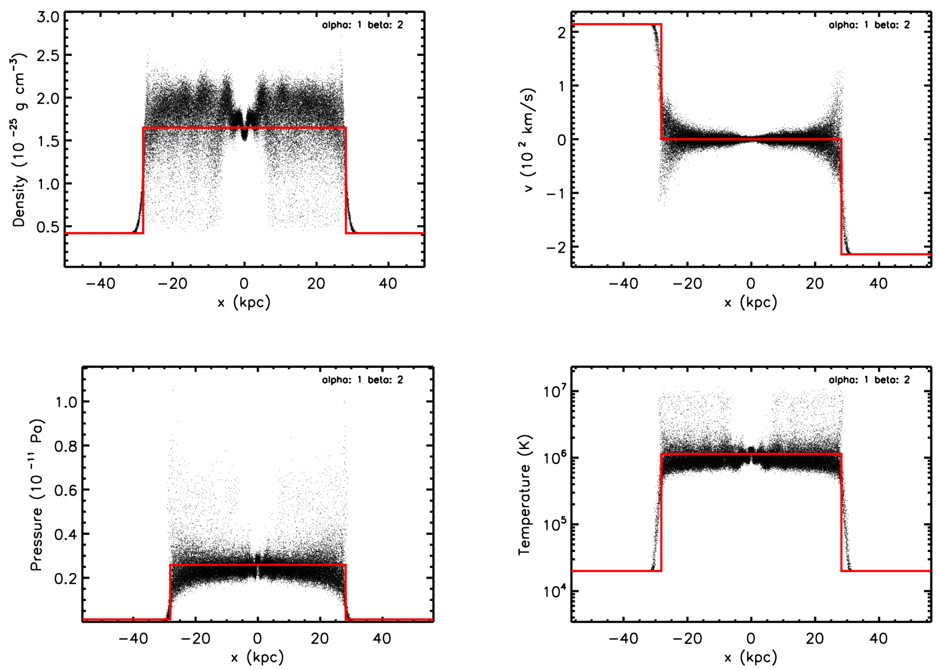

Figure 2.2: Standard colliding flow plots. All properties are *very* noisy. From left to right, top to bottom, we have density, velocity, pressure, and temperature.

We first consider our "vanilla" run; standard numerical values with no subgrid physics, seen in figure 2.2. It is immediately evident that the code behaves very poorly at such strong shocks. At the lower tested Mach numbers, the code produces very little noise in the shock tests that were performed. Performance shown in figure 2.2 for Mach 10 is not acceptable for simulations.

At first glance, it appears that some particles are managing to "plow" through the shock front and avoid shock heating, while others are essentially being "over-shocked." However, as will be seen later when single stepping is turned on, accuracy parameters don't seem to change behavior. This would suggest that it is extreme post shock oscillation. This is also supported by the fact that the extreme outliers decrease in magnitude towards the center of the box, where particles will have had time to damp oscillations, easily seen in the velocity plot, figure 2.2(b).

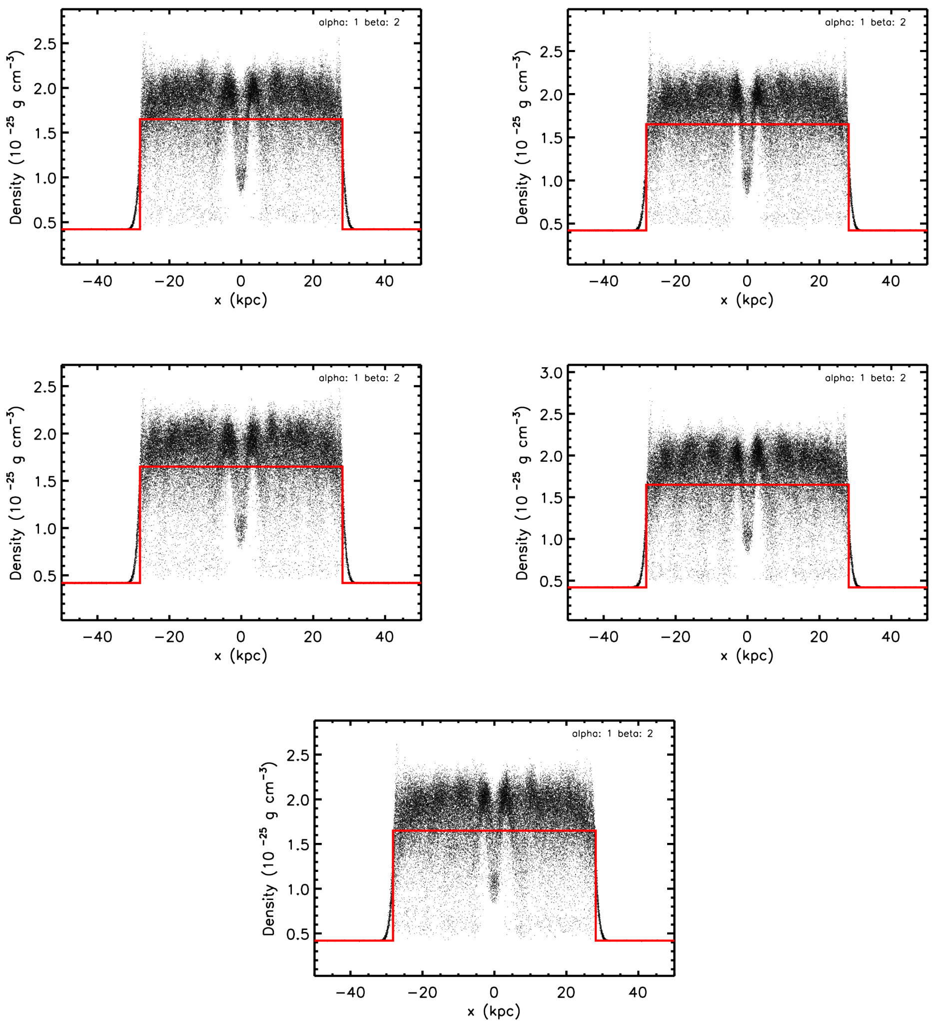

Figure 2.3: Increasing accuracy parameters in GASOLINE has no noticeable effect on the extreme noise. Only density is shown, but all other parameters exhibit the same lack of improvement. Going from top to bottom, left to right, we have changed the time step criterion (η), the courant time step criterion (η_{Courant}), the energy change limit ($\eta_{\dot{U}}$), single stepping, and all of the above at once.

Figure 2.3 shows the effect of numerical accuracy parameters. In these plots, η was changed from 0.175 to 0.1, η_{Courant} was changed from 0.4 to 0.2, $\eta_{\dot{U}}$ was changed from 0.2 to 0.05, and single stepping was changed from 0 to 1 (off to on). As is clearly seen, there is essentially no visible improvement in the noise for any parameter. Decreasing any of the above parameters essentially has the effect, directly or indirectly, of decreasing time steps of particles. This can pretty quickly add up to much longer simulations. It may be interesting to find out at what point, if any, these parameters start to help the shock behavior. However, this was not pursued as dramatically improved behavior was found by increasing the artificial viscosity coefficients. Figure 2.4 shows the shock behavior for a range of α and β.

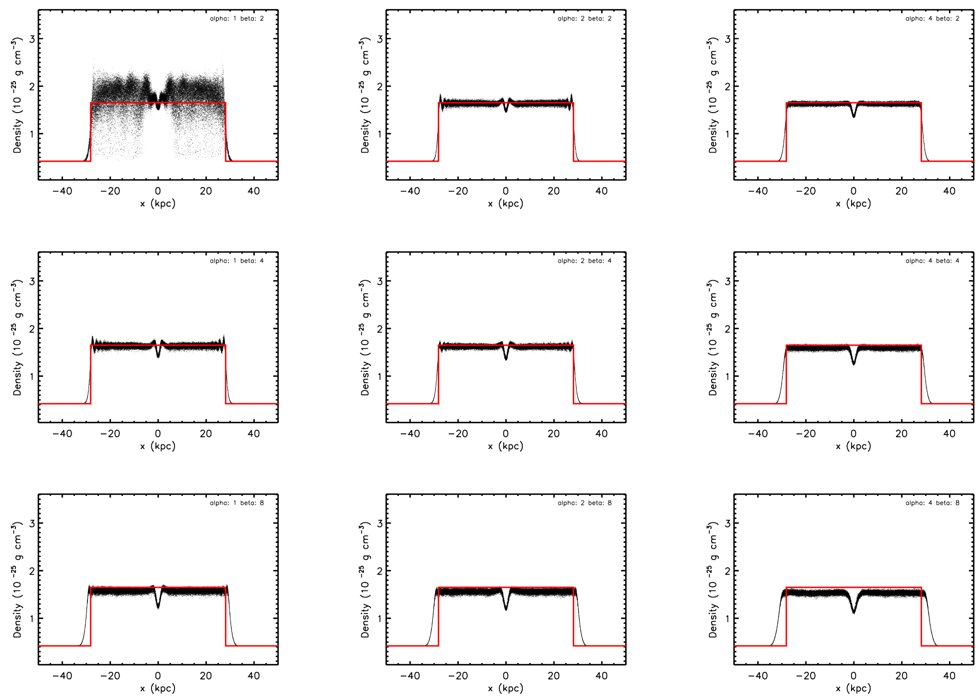

Figure 2.4: The effect of the viscosity coefficients on shock behavior. From left to right, α is 1, 2, and 4. From top to bottom, β is 2, 4, and 8. The best behavior appears to be $\beta = 2$ with $\alpha = 2$ or $\alpha = 4$.

Increasing the artificial viscosity terms knocks down noise very effectively. However, they have some side effects. Increasing either parameter leads to a thickening of the overall profile, especially post shock. As well, once the values are too high, the behavior starts to depart from the Riemann solution. This is seen as pre-shocking, where the fluid starts to feel the shock too early, and shock widening, where the shock front is artificially widened. Both effects contribute to a less accurate shock solution overall. While it is important to avoid extreme noise, as seen in figure 2.2, it is even more important to get an accurate solution to the shock. A balance in particle noise and shock accuracy must therefore be achieved. While not presented here, testing did show that the inaccurate shock solutions seen in the bottom row of figure 2.4 are likely due to incorrectly calculated time steps, and that increasing the accuracy parameters helped to improve this.

The two viscosity parameters tend to act on different parts of the shock. While both parameters seem to help reduce noise overall, the α parameter is much more effective at knocking down post-shock noise without affecting regions outside the shock. This is perhaps not surprising since the post shock environment is hot and dense, corresponding to high sound speed and low gas velocity. Since α acts on the linear velocity term, this is the region where it would tend to be dominant. On the other hand, β is more dominant in regions of high velocity, such as just outside the shock front or just after the shock front if there are extreme post shock oscillations. The effect is that post shock oscillations are reduced, but at the cost of pre-shocking the gas. It is therefore advisable not to increase β unless absolutely necessary. Huge improvements can be made simply by increasing α. These tests would suggest "best" values of $\alpha = 2$ or $\alpha = 4$, $\beta = 2$, different from the commonly adopted values of $\alpha = 1$, $\beta = 2$ (Monaghan, 1992), or $\beta = 2\alpha$ (Springel et al., 2001).

It is worth noting that many authors adopt the values of Monaghan (1992). It is likely true that the lower values of Monaghan (1992) are sufficient for 1-dimensional simulations, which is how most testing is done by Monaghan. However, SPH tends not to be as clean in three dimensions, and it appears higher viscosity is needed as shocks become more extreme.

The final parameter that was varied in the above tests was the viscosity switch. Most SPH codes use equation 2.14 as their switch, and by default so does GASOLINE. However, a newer switch has been developed by James Wadsley of the form

$$S_a = \frac{|\frac{\mathbf{dv}}{\mathbf{ds}}|_a}{|\frac{\mathbf{dv}}{\mathbf{ds}}|_a + |\nabla \times \mathbf{v}|_a + c_a/h}, \tag{2.20}$$

where dv/ds is the derivative of velocity in the direction of the gradient of density, c_a is the sound speed, and h is the smoothing length. The idea is that this turns the switch off for particle-particle pairs that happen to be moving towards each other, but not necessarily in an overall compressing flow. This should, in theory, reduce the noise in the switch. A comparison of the switches is shown in Figure 2.5.

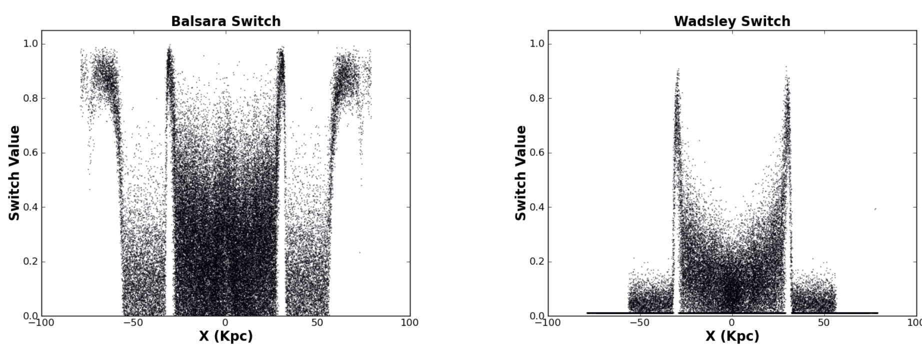

Figure 2.5: A plot of x vs the viscosity switch. Each point represents a particle in the tube. The shock is occurring at approximately ±30 kpc. While both switches are still noisy, the "Wadsley switch" is more clearly defined at the shock and lower overall throughout the box. It does not, however, make it to a full value of one, even at the shock.

The "Wadsley switch" seems to achieve its goal of more accurately identifying the shock. The shock front is more well defined by the switch, and the noise in the switch pre-and post-shock is certainly lower. The fact that the noise is lower after the shock means that viscosity will be lower in this part of the simulation. Since this is the region that experiences intense oscillations, this switch may actually impede the ability of viscosity to reduce the oscillations. The switch is further examined in a test with a different geometry in Section 2.3.6.

2.3.3 Cooled Flows Results

All testing done to this point has assumed an adiabatic gas model. This is the appropriate gas model in the limit of no cooling. However, most cosmological simulations these days, including Gasoline, involve cooling, and thus a more realistic test should include cooling.

With regards to galaxy formation, there are two regions where shock treatment is important; the edge of the hot halo of gas, and the edge of the disk. Gas accretion at the hot halo is discussed in section 1.3. The two regions have different average densities and thus different cooling rates. Cooling rate is approximately proportional to density, and thus gas accretion at the edge of the disk will have much shorter cooling times than gas at the hot halo. In order to incorporate both regimes, a range of densities has been tested, described in table 2.2. The four density runs using standard numerical parameters are presented in figure 2.6.

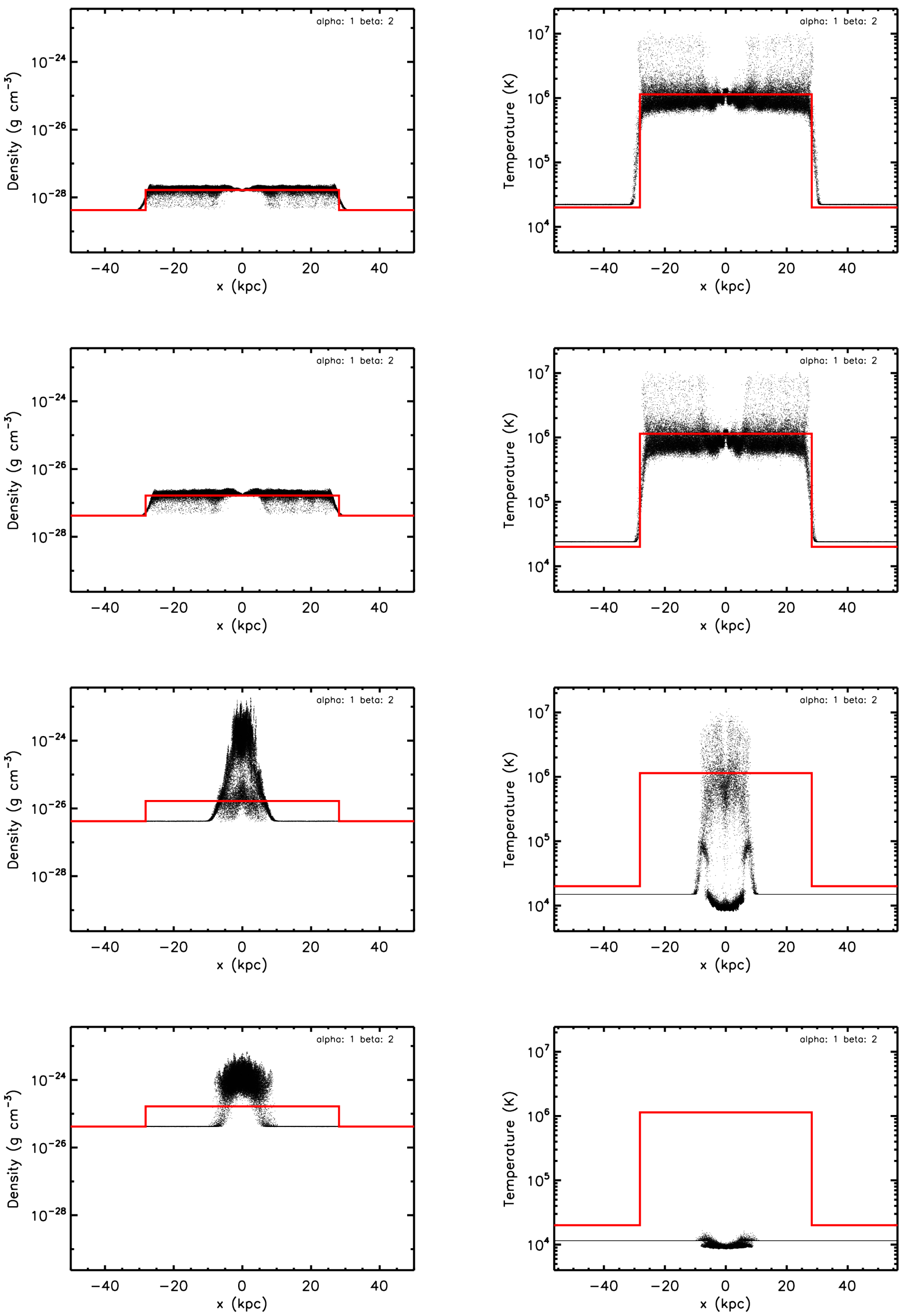

Figure 2.6: Shock profiles for the metal cooling runs. Column one and two are density and temperature, respectively. The rows go from density d1 to density d4 (see table 2.2).

In the limit of weak cooling, which corresponds to densities d1 and d2 (rows 1 and 2 in Figure 2.6), we see very similar behavior to the adiabatic tests run in section 2.3.2. The gas is not able to cool on a timescale similar to the shock formation and thus we see the same noise as before. These densities roughly correspond to the average density of the universe for medium to high redshift, so gas shocking at the hot halo may experience the same poor behavior that we see here. This is investigated in section 2.3.4.

In the case of extreme cooling, corresponding to d4 (row 4 in Figure 2.6), cooling happens at a much faster rate than heating from the shock, and so the gas cools as it decelerates and ends up as a cold, dense clump. This density approximately applies to regions within the disk of a galaxy. Gas that shocks within this region is thus likely to become very clumpy.

The most interesting case occurs at d3 (row 3 in figure 2.6). We see a distinct phase separation of particles in the shock. To understand why this is observed, it is helpful to look at the cooling curve for gas as a function of density and temperature, seen in figure 2.7.

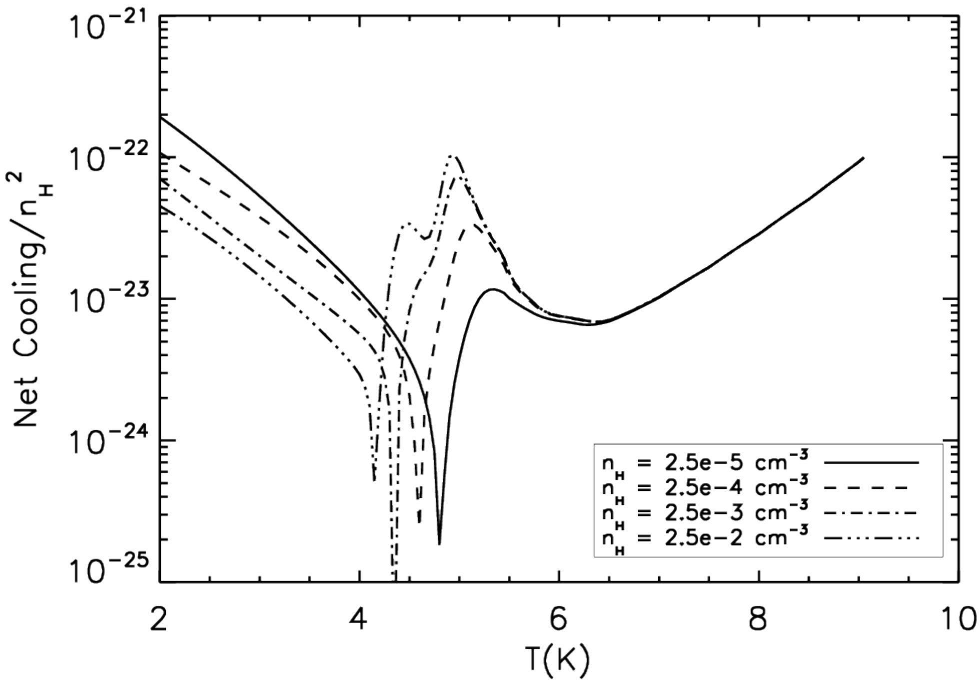

Figure 2.7: Net cooling rates calculated for specific densities. Figure provided by Sijing Shen.

It would appear that due to noise in the gas properties, some of the gas within the shock is able to make it over the hump in the cooling curve at 10^5-$10^{5.5}$ K, while other parts of the gas are not able to do so. This results in some of the gas quickly cooling and becoming dense on shorter timescales than shock heating, and the other part of the gas shock heating to the adiabatic solution temperature (equation 2.19), with cooling occurring on time scales longer than shock heating. It thus appears that there is an instability at play that favors a break up into hot and cold modes which is seeded by the noise in the solution.

This is a particularly interesting case because it represents an intermediate density found in the halo. Many recent simulations (e.g. Stinson et al. (2010); Guedes et al. (2011)), have found that cool clumps of gas seem to form while falling into galaxies, and may even form stars on the way in, and this may represent that exact regime. This phase instability is commonly called the Maller-Bullock instability, though Maller & Bullock (2004) achieve similar results by treating the hot and cold phases of gas separately from each other. In the case of Gasoline, the phase separation is an unintended side effect of numerical noise in an unstable region of density and temperature. Thus, improving particle noise within shocks in Gasoline may actually lead to a decrease in these cool clumps of gas.

These cool clumps of gas are important in the simulations because low entropy SPH particles have a tendency to avoid mixing and stay cool without some sort of diffusion, an unintended numerical issue. For this reason, it is likely that these cold clumps are not physical. While Gasoline does have diffusion implemented (Wadsley et al., 2008), it was not used in the cosmological runs.

2.3.4 Simulation Shock Front

This section jumps ahead a little and presents the shock fronts seen in actual cosmological simulations in order to compare to the testing done in sections 2.3.3. The details of the cosmological simulations are presented in chapter 3, but are not important to understanding the results presented below.

This analysis proved to be fairly difficult to do in a general way. While the theoretical idea that gas infalls, hits the hot halo at roughly the virial radius, and shock heats is roughly correct, it is not accurate enough to provide a definitive way of always finding the shock front in an output. As well, as can be seen in Figures 3.6, 3.7, and 3.8, the halo is not spherical, meaning that collapsing data down to the radial dimension introduces far too much noise. Thus, particular locations from specific outputs were hand picked in order to get the most comparable data to Section 2.3.

Figure 2.8 shows a box drawn around the region that was tested. There is a fairly substantial temperature jump across a relatively flat shock front, making it a good spot to compare to Chapter 2 results. The regions corresponds to a shock of approximately Mach 7.

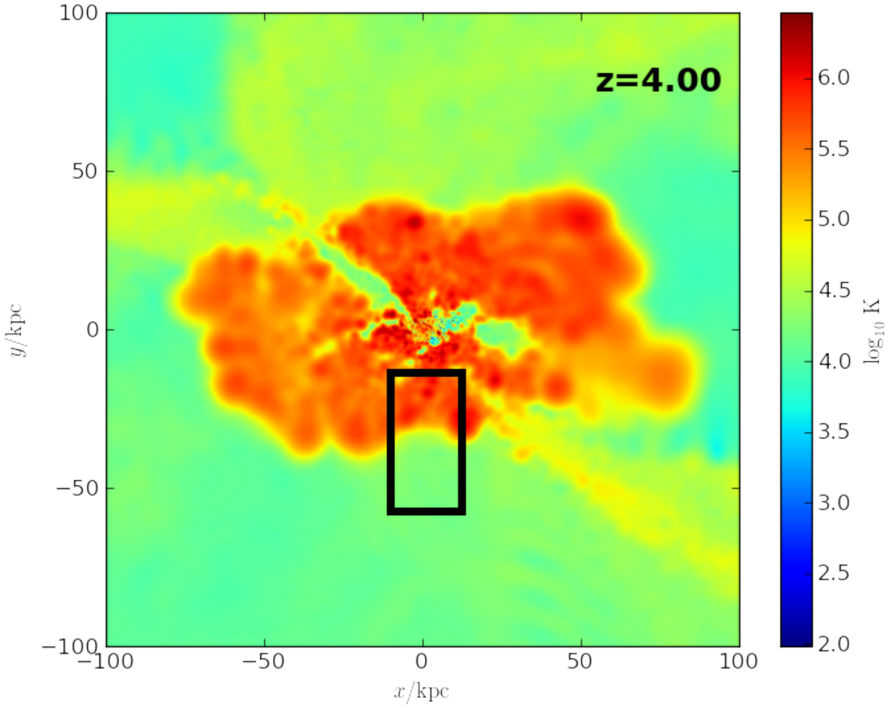

Figure 2.8: g15784, redshift 3 density plot. The boxed region represents where the shock front in figure 2.9 was plotted.

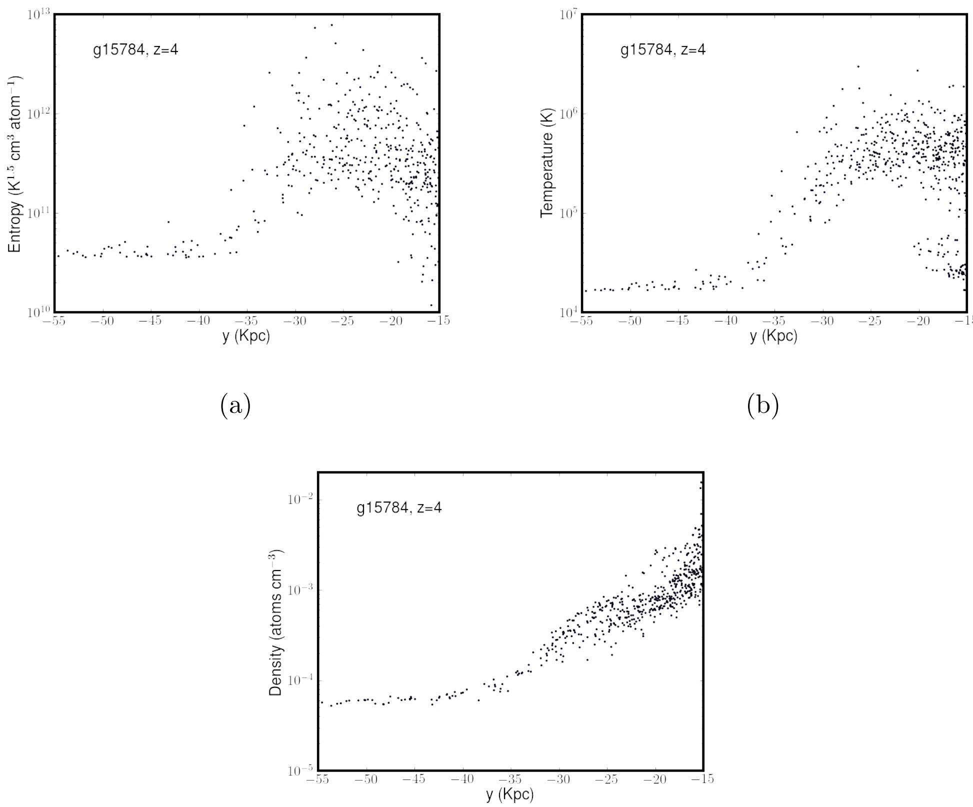

(a) (b) (c)

Figure 2.9: A shock front for g15784 at a redshift of 3. This corresponds to $-10 < x, z < 10$, shown in figure 2.8. From left to right, top to bottom, we have entropy, temperature, and density.

Figure 2.9 shows the shock front for density, temperature, and entropy, where entropy has been calculated as

$$S = \frac{T^{1.5}}{\rho}. \tag{2.21}$$

It is somewhat difficult to pin down exactly where the shock begins and ends since the gas is moving into a denser and hotter medium anyway, so an increase in these properties is expected. However, gas undergoing adiabatic compression should not exhibit a change in entropy, so the spot where entropy jumps should indicate fairly accurately where the gas leaves the regime of adiabatic compression and thus where it shocks. We can roughly pick this off of figure 2.9(a) as -37 kpc to -29 kpc, or in a region about 8 kpc wide.

At first glance, the shock front may seem overly wide. However, as we will see in the Evrard collapse (section 2.3.6), the shock is resolved with about 2-3 smoothing lengths (Figure 2.10, bottom right. The diamonds are spaced by smoothing lengths). The smoothing length at the shock front in figure 2.9 is approximately 2 kpc. Therefore the shock has been resolved in about 3-4 smoothing lengths, similar to previous testing.

Noise in temperature and density is lower but comparable to the testing from sections 2.3.2 and 2.3.3. Temperature has a spread of about an order of magnitude, while density has a spread of about a factor of four or five. This is certainly enough noise to cause phase separation similar to that seen in row 3 of Figure 2.6. Indeed, as we will see in figure 3.9, the blobs appear to be at the end of a cold filament stretching into the hot halo. These blobs may be gas particles that have shocked and separated at the edge of this cold filament.

2.3.5 Evrard Spherical Collapse Test

The spherical collapse test consists of an initial spherical cloud of gas set up with a shallow density profile of $\rho \propto r^{-1}$. The initial temperature is set far below the the virial temperature of the cloud (Evrard, 1988). In our case, T was approximately $T_{\mathrm{vir}}/20$. The cloud is then allowed to collapse under its own gravity. Because the temperature is much below the virial temperature, the collapse happens on essentially one free-fall time and creates an outward moving shock front as material from the outer radii hits the dense core.

This test was used to see the effect of increasing α in a slightly more realistic shock scenario. We have run the testing for standard gasoline parameters and for increased α values, as well as with a modified viscosity switch (see section 2.3.1, equation 2.20). Results are then compared to high resolution results for the one-dimensional version of the initial conditions run with a very accurate Particle-Particle-Mesh (PPM) method (Steinmetz & Mueller, 1993).

2.3.6 Evrard Collapse Results

The adiabatic collapse of Evrard (1988) provides some important insight into the effects of viscosity. While the shock tubes do a good job demonstrating the issues associated with capturing shocks, an adiabatic collapse is more similar to actual astrophysical simulations. As well, because particles are all collapsing towards a point rather than towards a plane, any viscosity issues should be amplified. Figure 2.10 shows the standard gasoline run with no changed parameters; this is the same as figure 9 from Wadsley et al. (2004). As with Wadsley et al. (2004), density, pressure, entropy, and velocity are in units of $\rho_* = 3M/4\pi R^3$, $P_* = \rho_* \epsilon_* = 3GM^2/4\pi R^4$, $S_* = P/\rho^\gamma$, and $v_* = \sqrt{GM/R}$, respectively. Note ϵ_* in energy, GM/R. Figure 2.11 shows the effect of varying the α parameter and the viscosity switch. The left column contains the standard switch (equation 2.14), and the right column contains the Wadsley switch (equation 2.20). The first row shows $\alpha = 2$, and the second row shows $\alpha = 4$.

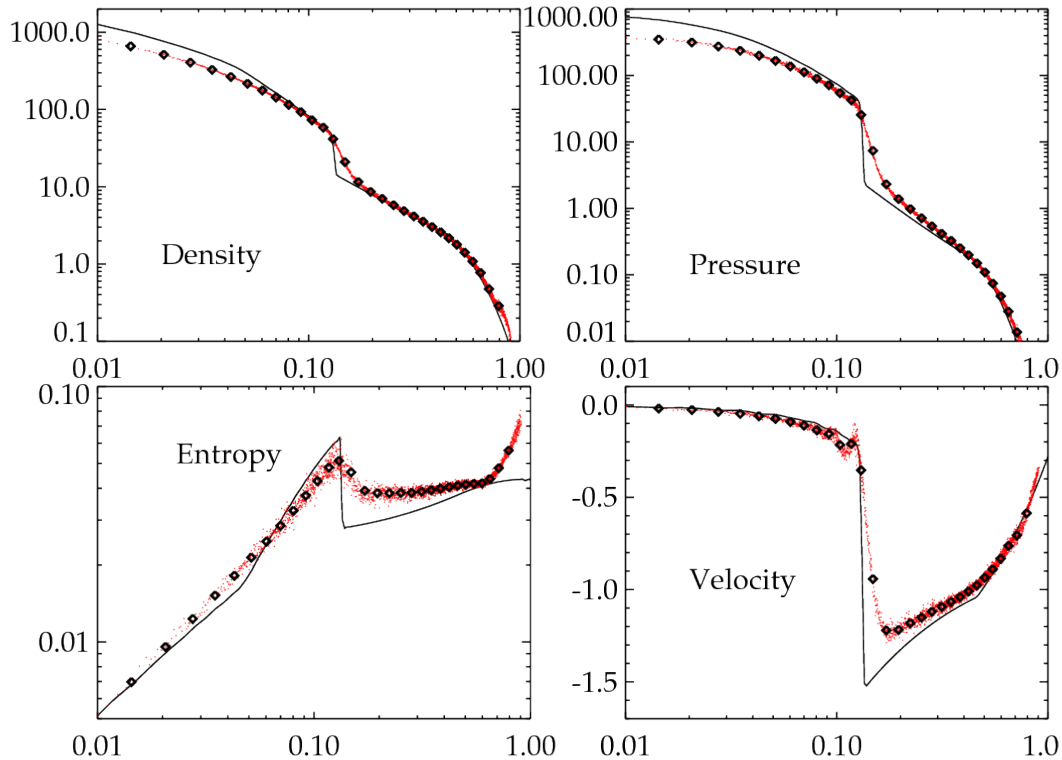

Figure 2.10: The adiabatic collapse test with standard parameters.

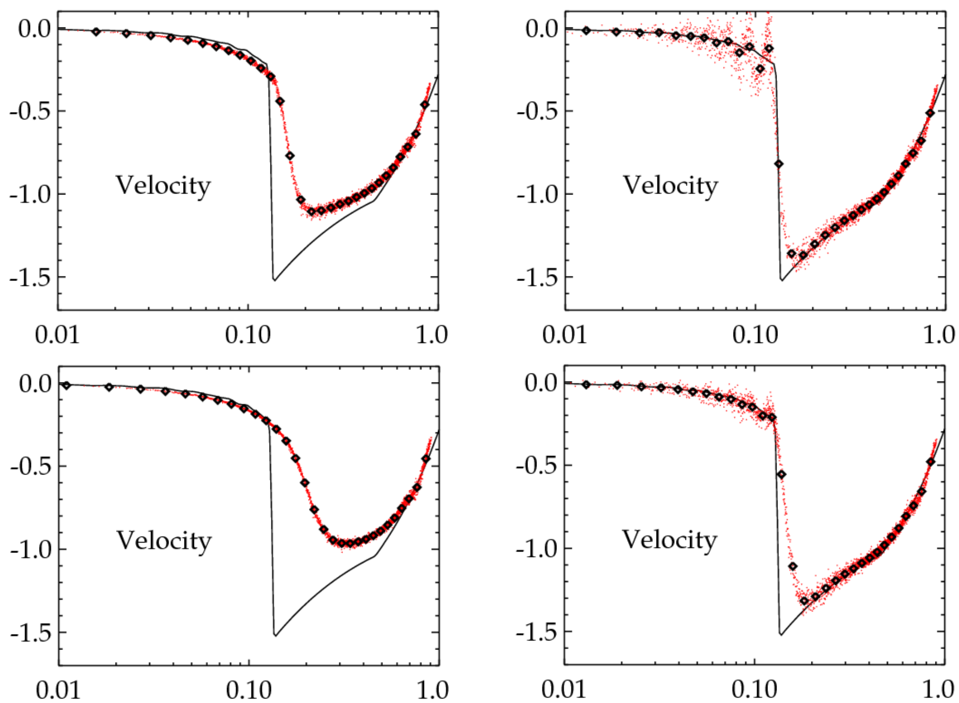

Figure 2.11: Velocity of the particles for the adiabatic collapse test in which the viscosity switch and α have been varied. Column 1 uses the regular viscosity switch, and column 2 uses the Wadsley switch. Row 1 uses $\alpha = 2$ and row 2 uses $\alpha = 4$. The effects of increasing α quickly lead to severe pre-shocking in the colalapse. Using the Wadsley switch creates a very accurate shock front, but post shock noise dramatically increases.

Figure 2.11 demonstrates the problem with increasing viscosity parameters. If viscosity is too high in regions where it should not be, pre-shocking can become very bad. The Wadsley switch does a fantastic job at preventing pre-shocking. In a spherically symmetric system, this switch would have a huge benefit, as only particles compressing in the radial direction would have viscosity applied. However, it turns off immediately after the shock and thus post-shock oscillations are severely problematic, even with the increased viscosity. For this test case, our best solution is actually the standard run (figure 2.10). Some codes have adopted an approach that does not allow alpha to turn off quickly, but actually lets it exponentially die off (Morris, 1997). An approach of this sort could be hugely beneficial for shock treatment in GASOLINE.

2.4 Closing Thoughts on Testing

It is certainly difficult to treat shocks properly. After all, they are essentially discontinuous features of fluid flow; not easy phenomena to model. However, the testing presented in this chapter has given some insights. Shocks of astrophysical scale are not, in general, treated very well. Post shock oscillation can be a serious problem that accuracy parameters don't seem to help, at least not in the tested, and admittedly small, range of parameter values. Increasing the linear coefficient in viscosity, α, may help, but it is not the ideal fix as it worsens pre-shocking. The modified viscosity switch shows huge improvement over the traditional switch in tracking the shock, but actually leads to worse post-shock behavior.

It is important to keep in mind how these effects manifest in cosmological simulations. These simulations typically involve gravitational collapse, and so it is tempting to weight the results from the adiabatic collapse test more heavily, which suggest leaving the parameters how they are. However, the location of the shock in the simulation is important. Gas shocking at the edge of a halo is on a large enough scale that it may still be quite similar to the colliding flows test. That being said, gas shocking (or failing to shock) at the boundary of a cold flow and the galactic disk may be more similar to the Evrard collapse. These scenarios will be considered in chapter 3.

Chapter 3

Cosmological Runs & Results

3.1 The McMaster Unbiased Galaxy Simulations (MUGS)

The McMaster Unbiased Galaxy Simulations (MUGS) is a suite of simulations that aims to better understand aspects of galaxy formation through examination of a large, unbiased sample of galaxies simulated at high resolution (Stinson et al., 2010). To date, sixteen galaxies have been simulated within a mass range of $4.5 \times 10^{11} M_{\odot}$ - $2 \times 10^{12} M_{\odot}$ using GASOLINE (section 2.2). Physics in the MUGS runs include metal cooling, UV background heating, star formation, and stellar feedback (section 2.2.1).

The MUGS galaxies were selected from an initial DM-only simulation using 256^3 particles in a 50 h^{-1} Mpc box. The simulation was a subsampling of a 4096^3 version with a CMBFAST (Seljak & Zaldarriaga, 1996) power spectrum. Cosmological parameters were taken from the WMAP3 ΛCDM cosmology (Spergel et al., 2007), and are shown in table 3.1.

Table 3.1: WMAP3 parameters used for MUGS.

Parameter	**Value**	**Parameter**	**Value**
H_0	73 km/s/Mpc	Ω_b	0.04
Ω_m	0.24	σ_8	0.76
Ω_Λ	0.76		

Once at redshift zero, group finding was performed using a friends-of-friends algorithm to find virialized halos. All halos between $5 \times 10^{11}\ M_\odot$ and $2 \times 10^{12}\ M_\odot$ were identified and checked to ensure that they did not evolve closer than 2.7 Mpc to any halo more massive than $5 \times 10^{11} M_\odot$. This ensured that adding gas to the run will not result in a drastically different halo from that in the DM-only run. Out of the remaining 276 halos, galaxies were randomly chosen to re-simulate with gas.

Initial conditions for each galaxy were created using the zoom renormalization technique (Governato et al., 2004). Particles within $5r_{vir}$ of the particular galaxy in the DM-only run were tracked back to the initial condition, and the region those particles occupied was defined as the region of interest. Within this region, DM particles were filled in on a regular grid to create an effective resolution of 2048^3. Outside this region, a spherical region with radius 1.2 times the maximum radius of the region of interest was created with an effective resolution of 512^3. At three more equally spaced radii outside this region, particles were filled in with effective resolutions of 256^3, 128^3, and 64^3. The leftover region in the box was filled in with an effective resolution of 32^3.

Within the region of interest, all dark matter particles were split to form a gas particle with mass equal to Ω_b/Ω_m. Finally, the particles in each region were perturbed using the Zel'dovich approximation (Zel'Dovich, 1970). Within the high resolution region, DM particles have a mass of $1.1 \times 10^6\ M_\odot$ and gas particles have a mass of $2.2 \times 10^5\ M_\odot$. DM particles outside of the region have multiples of this mass equal to the decrease in resolution. Particles were given a gravitational softening length, ϵ, of 312.5 pc.

Separate from MUGS, a higher resolution version of the DM-only simulation was run with effective resolution of 512^3. This was done in order to check how distribution properties of the halos in the simulation changed with resolution. Specifically, the mass function and spin parameter distribution of each simulation was checked for consistency.

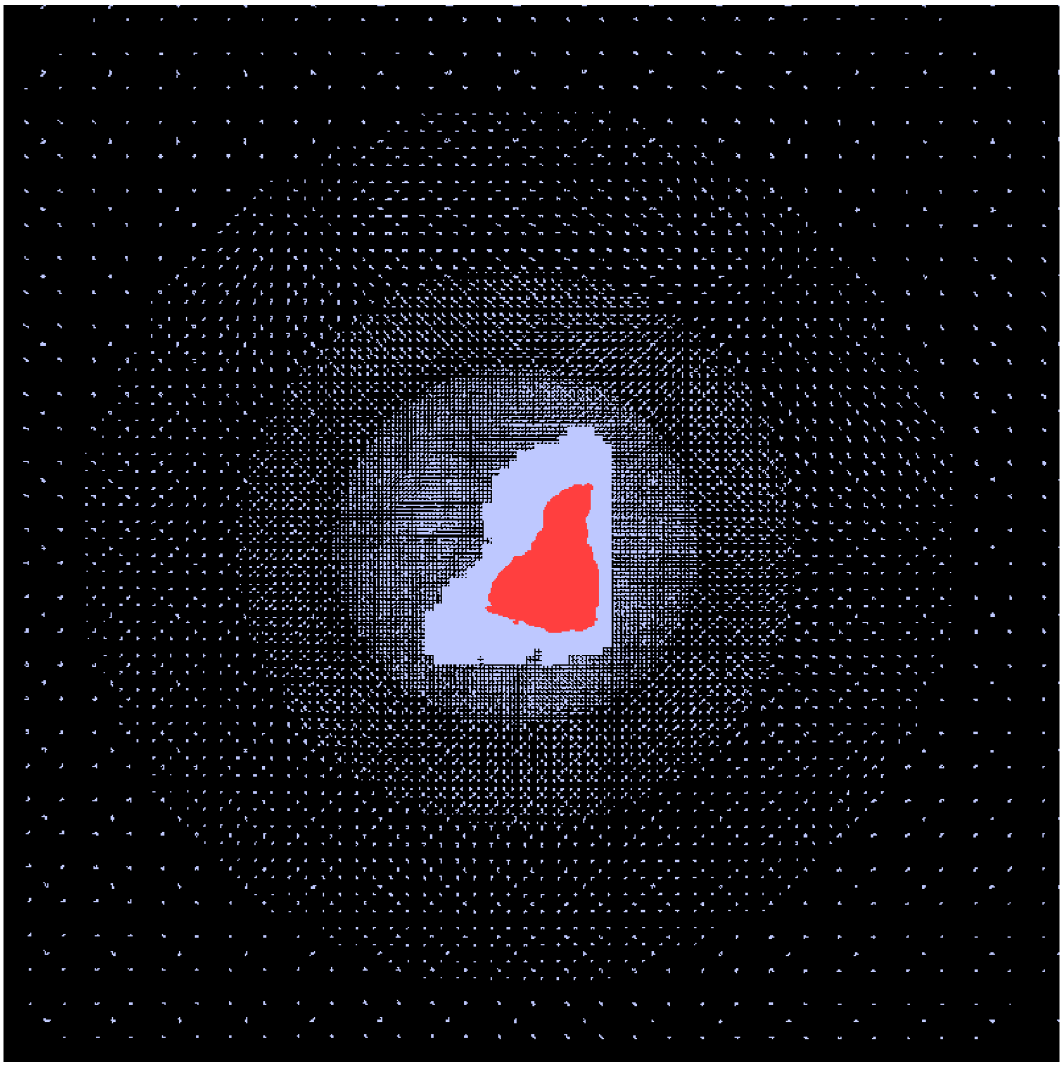

Figure 3.1: A view of the initial condition for g15784. The region of interest is shown in red (gas), and the blue is dark matter. The resolution in the spherical regions outside of the region of interest is easily seen to decrease. Figure created by Greg Stinson.

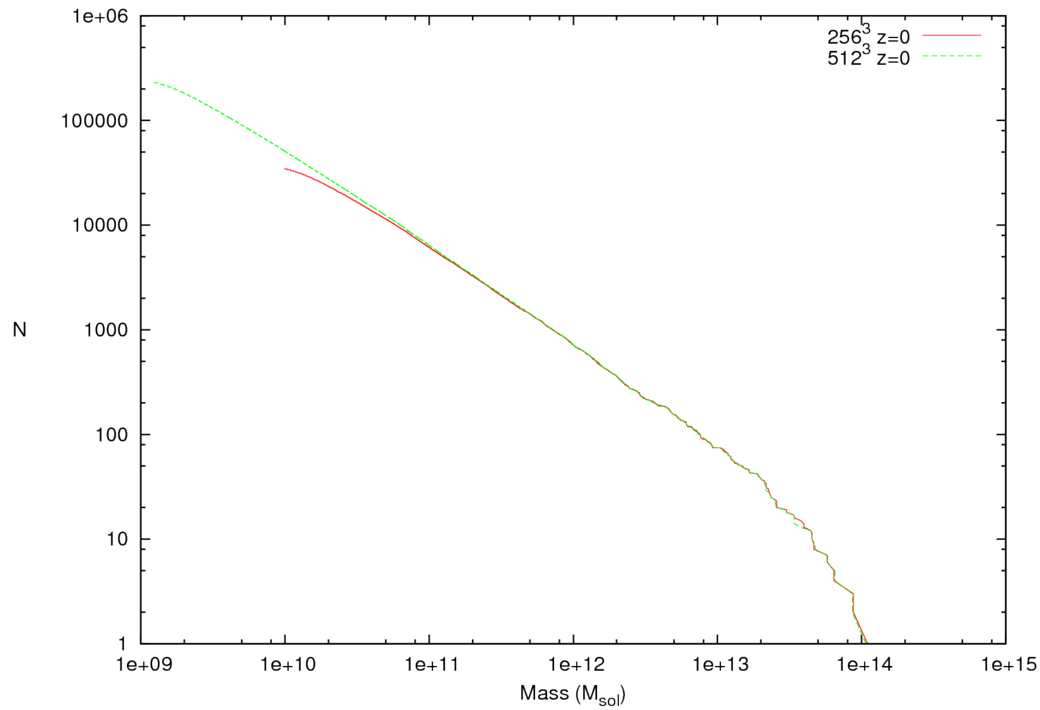

Figure 3.2: The mass function of the two DM-only simulations. We can see that both mass functions agree, and that 512^3 simulation goes about eight times lower in mass due to eight times higher resolution.

For any galaxy, the spin parameter is a dimensionless quantity that gives a rough estimate of the total amount of kinetic energy that is contained in rotation of the galaxy (Peebles, 1969),

$$\lambda = \frac{J|E|^{1/2}}{\sqrt{G M^{5/2}}}, \tag{3.1}$$

where J is the total angular momentum of the halo, G is the gravitational constant, M is the virial mass, and E is the total energy.

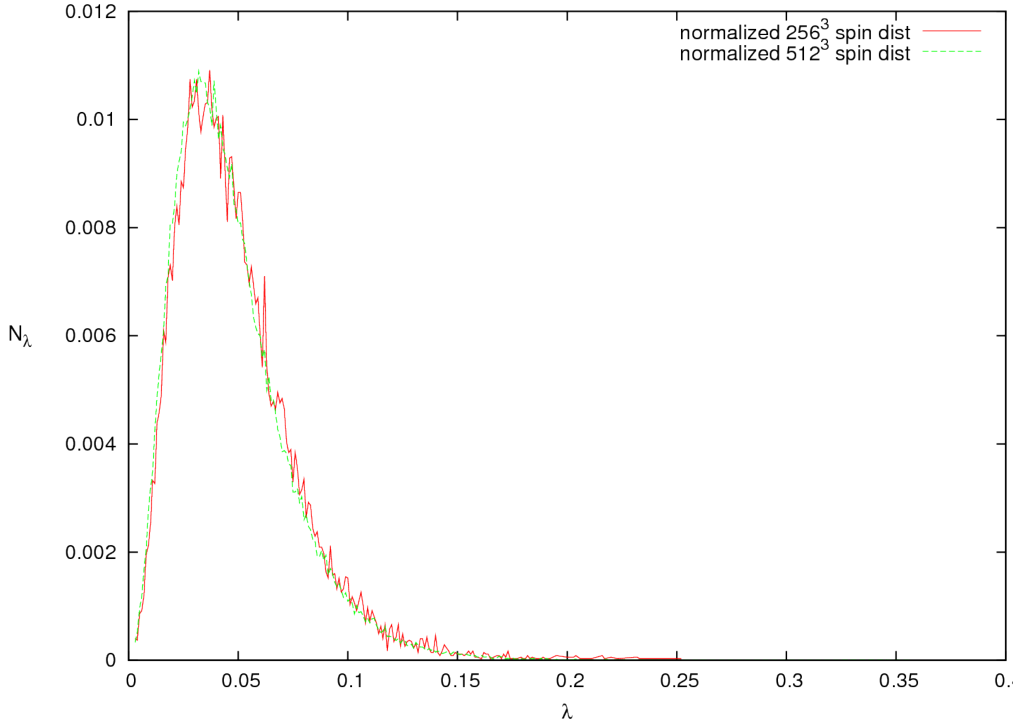

Figure 3.3: The distribution of spin parameter, λ, normalized by total number of halos. Both distributions agree, though the lower resolution run is more noisy, as expected, due to the lower number of total halos.

Figure 3.2 shows the mass function and figure 3.3 shows the spin parameter distribution normalized by total number of halos. Both plots show agreement in global properties. As well, figure 3.2 shows that the lower resolution simulation does not depart from the mass function of the higher resolution run until below $1 \times 10^{11}\ M_\odot$, suggesting that the original DM-only simulation was of sufficient resolution to characterize halos in the chosen mass range.

Results from Stinson et al. (2010) suggest that MUGS in general make too many stars and end up with overly large bulges. This is easily seen as a large central peak in the rotation curves of the galaxies. However, most of the galaxies still end up within observed relations such as the Tully Fisher relation and within the observed color-magnitude diagram from the sample of Sloan Digital Sky Survey (SDSS) galaxies, suggesting that qualitative behavior is pretty good. Since the analysis in this chapter will focus on the "how" of star formation and gas accretion rather than the exact amount of star formation, the results presented here should not be strongly affected by these issues.

3.2 Selected Galaxies

From the MUGS project, we selected four galaxies to analyze. The names of the galaxies and the properties of each galaxy are presented in table 3.2.

Table 3.2: Sample of z=0 galaxies used from MUGS for analysis. λ is the spin parameter, and N_x is the number of particles of type x.

Galaxy	Mass ($M_\odot$)	λ	N_{gas}	N_{star}	N_{dark}
g7124	5.0e11	0.039	1.4e5	1.2e6	3.7e5
g25271	1.4e12	0.0144	4.6e5	2.4e6	1.1e6
g15784	1.5e12	0.0345	5.3e5	2.6e6	1.2e6
g15807	2.3e12	0.023	8.7e5	4e6	1.7e6

The galaxies in our sample were selected for a couple of reasons. g15784 was the first galaxy to be selected due to its "nice" properties. It is a stable galaxy with a fairly quiet merger history and a fairly high star formation rate early in its history. At z = 0, it has a well-defined disk and most of the properties match pretty well with the spread of observed galaxies (Stinson et al., 2010). The following three galaxies, g7124, g25271, and g15807, were selected to straddle the approximate mass limit for shocking ($10^{11.6}$ $M_{\odot}$, e.g. Brooks et al. (2009), explained in Section 3.3) and to still be realistic galaxies with a spread in properties such as λ and merger history. See table 1 of Stinson et al. (2010).

3.3 Included Analysis

Over the past decade, a number of papers have made important modifications to the standard view of gas accretion in galaxies. Birnboim & Dekel (2003) showed that a stable shock could not actually be supported below a characteristic mass, and that most of the gas would accrete in the cold mode. Kereš et al. (2005) and Dekel & Birnboim (2006) highlighted the importance of stream-fed gas accretion, and noted that a lot of cold gas is delivered in this way. Ocvirk et al. (2008) added that metallicity is an important parameter to determining the characteristic mass at which halos can support a stable shock. Finally, Brooks et al. (2009) characterized that a comparable amount of gas could be accreted in the cold mode, and that star formation in the disk of galaxies was generally dominated by this cold gas accretion.

Most of the above papers note that the cold flows are generally easily seen by making cuts in either temperature, density, entropy, or some combination of the three. Stewart et al (2011a,b) make the link to observations, suggesting that cold mode accretion should be visible in absorption-line studies, especially at higher redshifts where the covering fraction of the cold gas is much higher .

The goal of analysis presented here was to further characterize accreting gas and to get an idea of how the accretion mode affected star formation.

For each galaxy, a number of different analyses were performed. At each output, halo finding was done in order to identify the main halo and all particles bound to it. The Amiga Halo Finder (AHF, Knollmann & Knebe (2009)) is a parallel halo finding program that identifies substructure using an adaptive mesh. Each cell has a density calculated and substructure is identified based on density contours. From here, all particles within a density contour are checked for boundedness by calculating the escape velocity at each particle's position. Unbound particles are then removed from the halo. This procedure occurs at all density contours, and so AHF is excellent for finding halos and substrucuture of halos.

In order to get a qualitative idea of what was happening in the simulation at each step, property maps were made for the galaxy oriented face-on and edge-on for density, temperature, Mach number, balsara switch, entropy, and mass inflow rate. These were used to help identify outputs of interest and give a qualitative view of gas inflow.

Quantitative analysis included temperature-density phase diagrams and radial velocity-temperature diagrams, all done at concentric spherical shells out to 2 virial radii (section 3.5). As well, star particle tracking was done in which the parent gas particle for every star particle was tracked back in time to its accretion onto the galaxy. Gas properties were recorded for each particle at all times it was found between 0.2 and 1 virial radii. This enables a star formation history to be split up based on whether the gas came from cold or hot mode accretion (section 3.6). Finally, density profiles were created for thin shells at the virial radius of the halo to look at the shock profile of the accreting gas (section 2.3.4).

All data analysis and images were done using the PyNBody package[1] for version 2.6 of the python programming language.

3.4 Qualitative Behavior

A mass history for each galaxy has also been created by recording the total mass of all particles found to be bound to the main halo by AHF. These give a rough idea of important redshifts where large mergers occur and important masses are reached. The mass histories are presented in figure 3.4.

[1] http://code.google.com/p/pynbody/

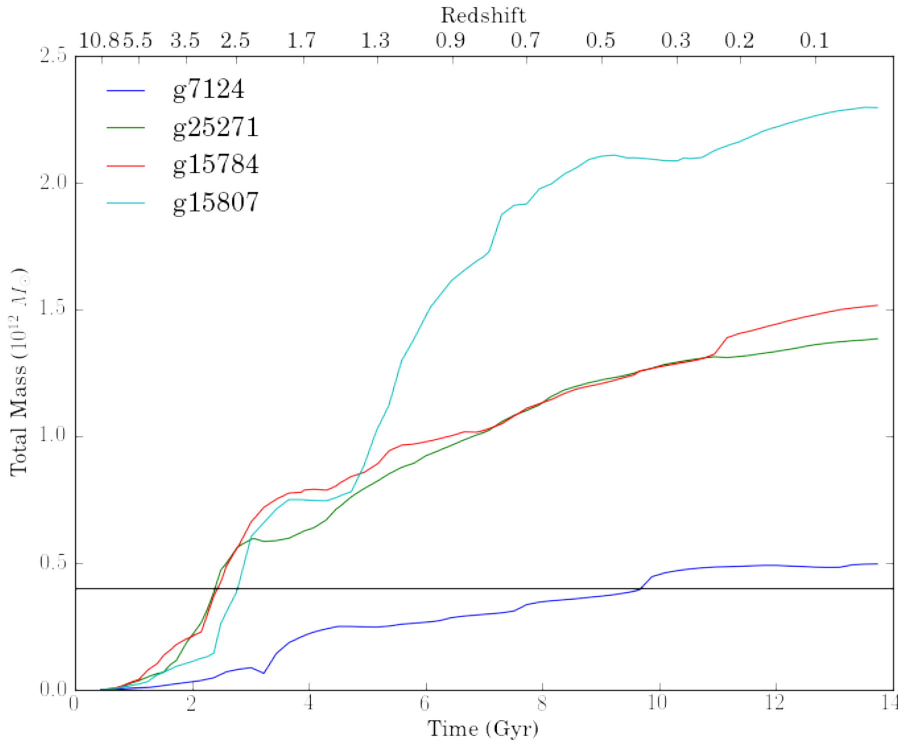

Figure 3.4: Mass histories for the galaxies. The horizontal line is drawn at M = 1e11.6 $M_{\odot}$, the approximate mass at which galaxies can support a stable shock (Brooks et al., 2009).

We see that the 3 largest galaxies all cross the mass threshold to support a stable shock early on in their history, around a redshift of 3. Both g25271 and g15784 have fairly quiet merger histories, with gradual growth through accretion after a redshift of about 2. g15807, the largest galaxy, has a very active growth rate until a redshift of about 0.5. The smallest galaxy, g7124, has a fairly quiet history except for a decent sized minor merger at a redshift of about 0.4.

In order to get an idea of where interesting events are happening, property maps were created at all outputs between redshift 4 and 2, with density and temperature maps made at all simulation outputs. Each map has been done for an edge on and face on view of the galaxy at various radii. All maps represent slices through the z=0 midplane. A small number of interesting maps have been selected to present here.

Figure 3.5 shows a range of properties for the galaxy g15784 at redshift 3. A cold inflow of gas can be easily seen in most of the properties on the left side of the image, and a less distinct one is seen on the right side. These cold flows are seen as "fingers" stretching from outside the hot halo into the inner regions of the galaxy. They are dense and cold (3.5(a),3.5(b)), and have a lower entropy than even the gas surrounding the hot halo (3.5(c)). This is due to the increased cooling rate in the denser region. The gas travels in at a very high Mach number because of the low sound speed and high gas velocity (3.5(d)). Finally, we see that the Balsara switch (3.5(e)) is very low in this region, suggesting that the gas is smoothly flowing without shocking.

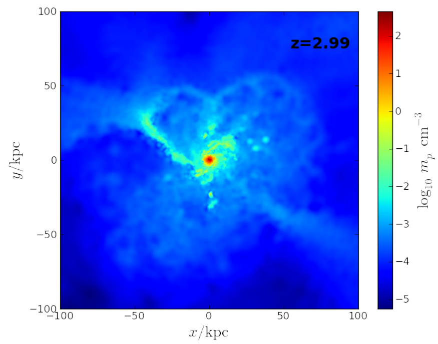

(a) Density

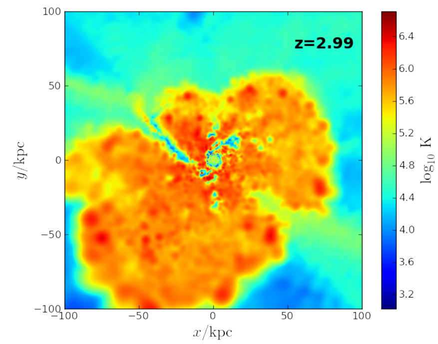

(b) Temperature

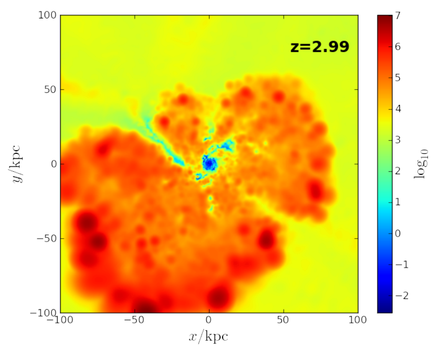

(c) Entropy

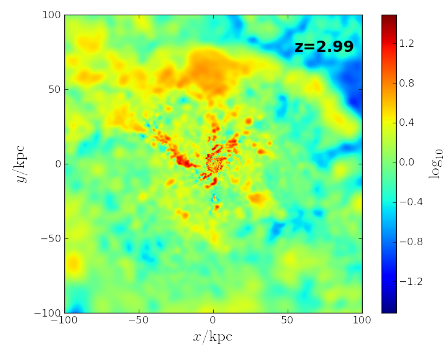

(d) Mach Number

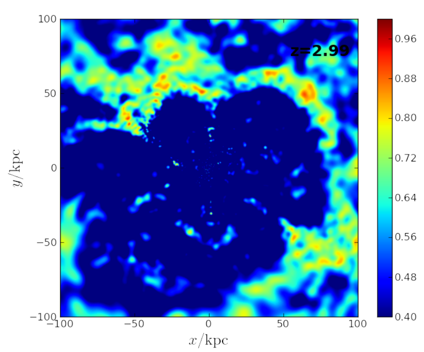

(e) Balsara Switch

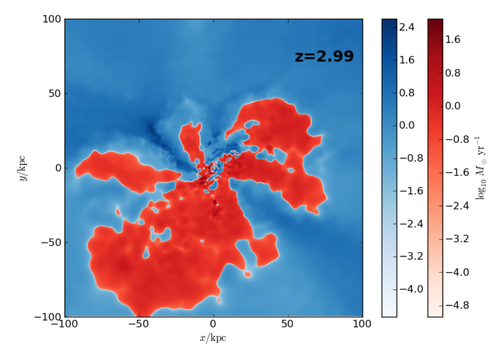

(f) Mass Flow Rate

Figure 3.5: Property maps at redshift 3 for g15784. From left to right, top to bottom, the properties are density, temperature, entropy, Mach number, Balsara switch, and mass flow rate. The flow rate map has a blue scale for inflow and a red scale for outflow.

A series of gas density images and DM particle locations over time are plotted in figures 3.6 and 3.7. This series shows that the cold flow of gas is persistent over many gigayears, and stays essentially where the DM filaments are. The cold flow eventually seems to break up at a redshift between 2.9 and 2.7.

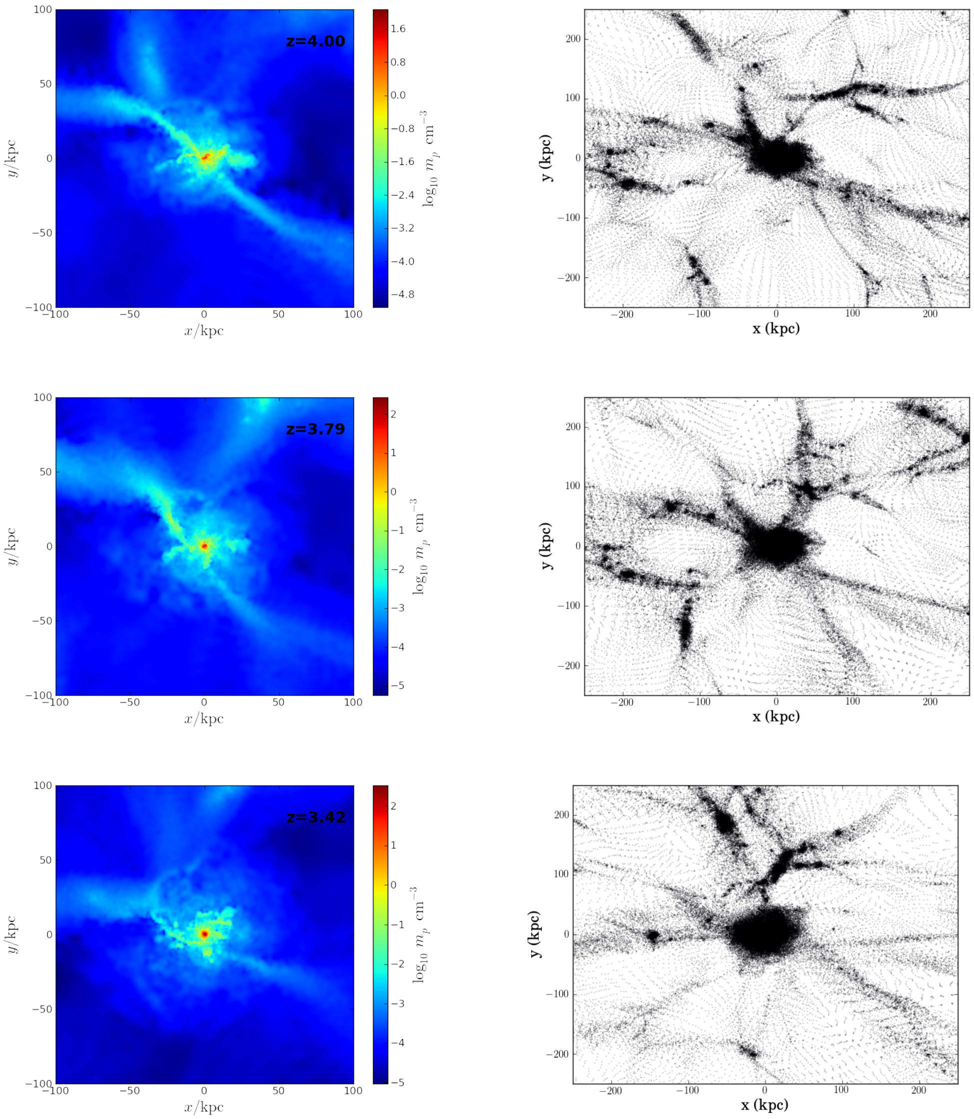

Figure 3.6: A time series (I) of density and DM images for g15784. The cold flow is easily visible up until a redshift of about 2.75, at which point it appears to collapse.

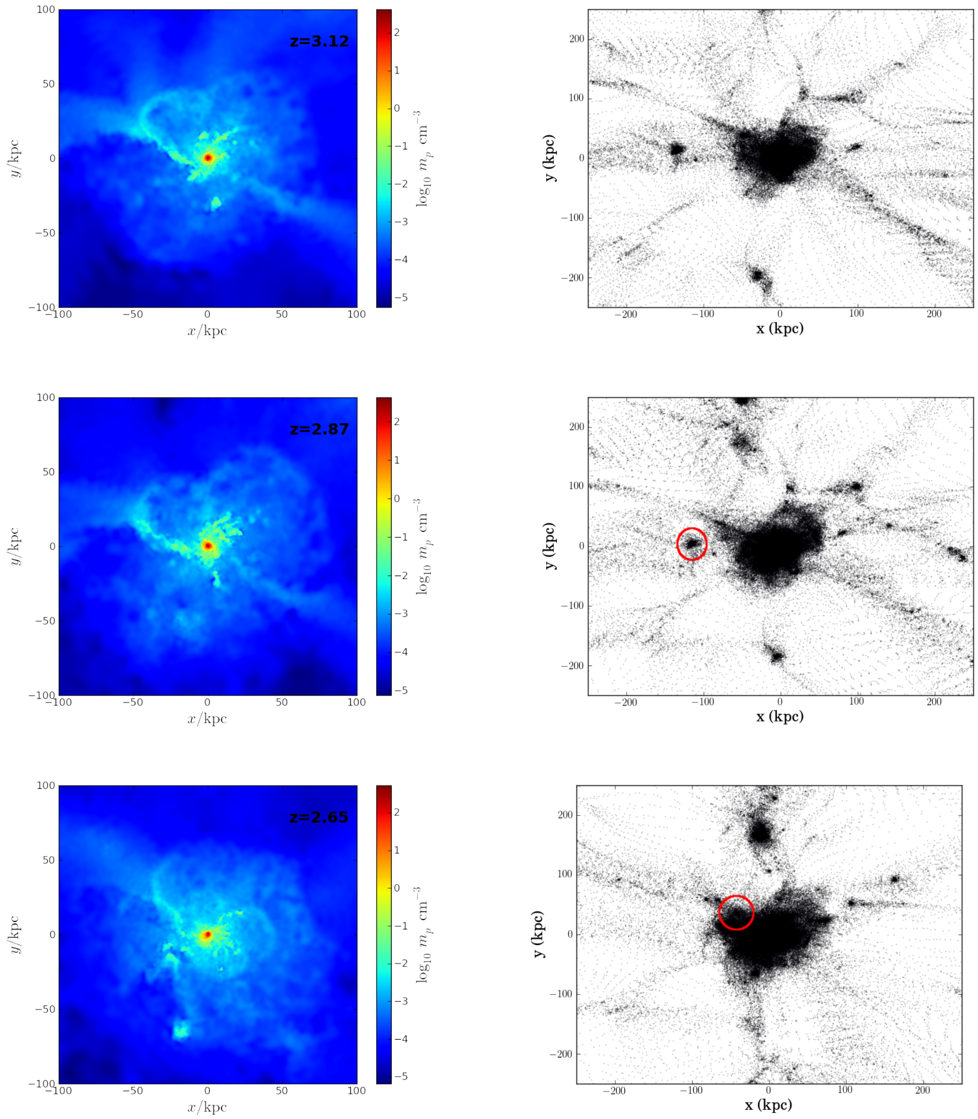

Figure 3.7: A time series (II) of density and DM images for g15784. The cold flow is easily visible up until a redshift of about 2.75, at which point it appears to collapse. In panels 3.7(d) and 3.7(f), a small DM halo is circled that appears to break the main cold flow upon accretion.

It is clear that the galaxies are stream fed in all of the cases. All of the galaxies seem to accrete gas along filaments from quite large radii, in agreement with the literature (Birnboim & Dekel, 2003; Kereš et al., 2005; Dekel & Birnboim, 2006; Kereš et al., 2009; Ocvirk et al., 2008; Dekel et al., 2009; Brooks et al., 2009; Stewart et al., 2011). Early on in the history, the filaments penetrate fairly deeply into the galaxy. As time passes, the filaments appears to collapse, meaning the efficiency of gas delivery to the disk decreases. This "typically" occurs (in our samples) between a redshift of 1 and 3 depending on the galaxy. In this case, it appears that a small DM halo may have actually broken the filament as it was accreted (the small halo has been circled in Figure 3.7). However, in general it is still unclear what this collapse of the filament is primarily due to. Further investigation is needed into this matter.

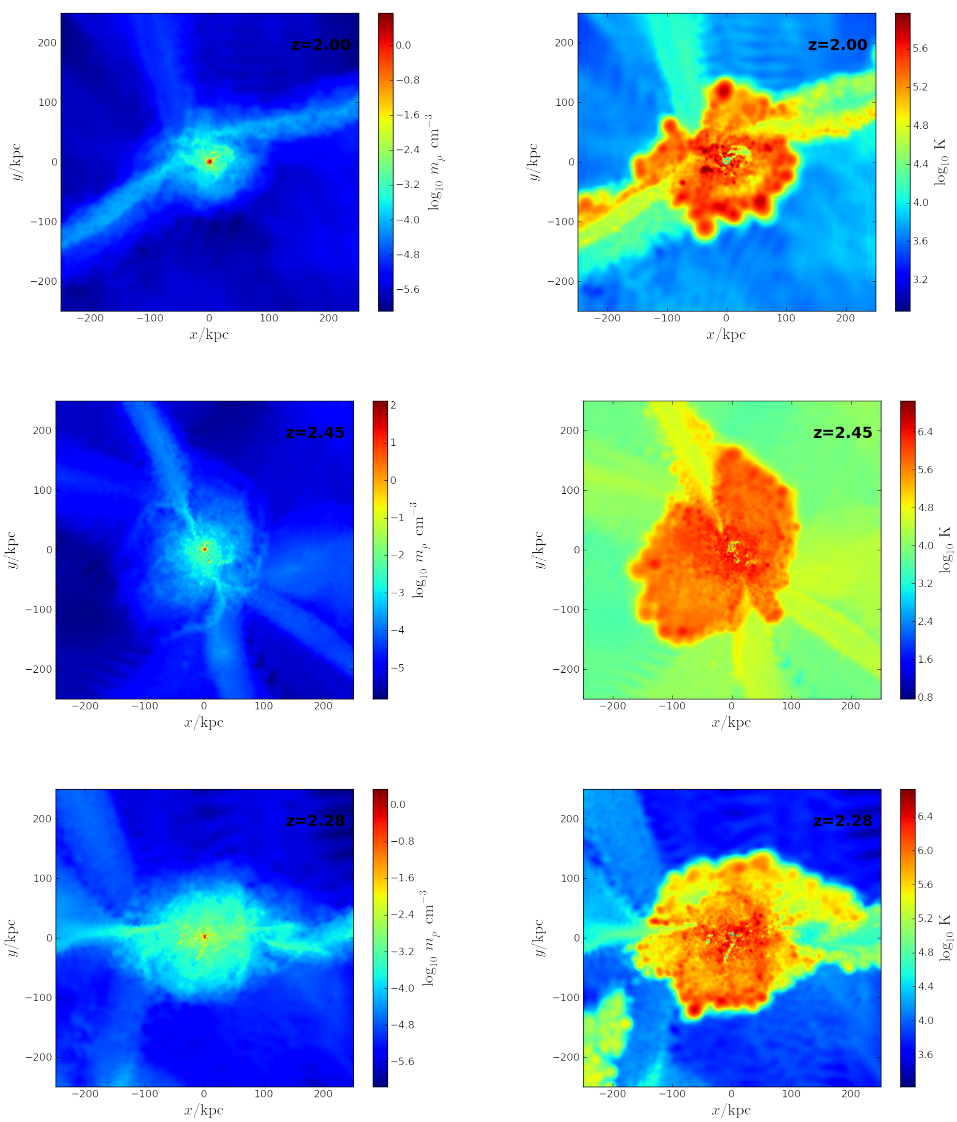

Figure 3.8: Density and temperature maps for the other studied galaxies. The left column is density, the right column is temperature. From top to bottom, the images are of g7124, g25271, and g15807.

At lower redshifts, typically between about 2 and 0.5, many of the galaxies exhibit the cool blobs mentioned in chapter 2. These blobs are circled in figure

3.9. Unfortunately, due to limited time resolution between outputs, it's difficult to get an idea of how long these blobs persist. From an analytic standpoint, cool clumps of gas in a warm flow should break apart relatively quickly. However, without diffusion, these blobs can persist for quite a while in SPH (Agertz et al., 2007).

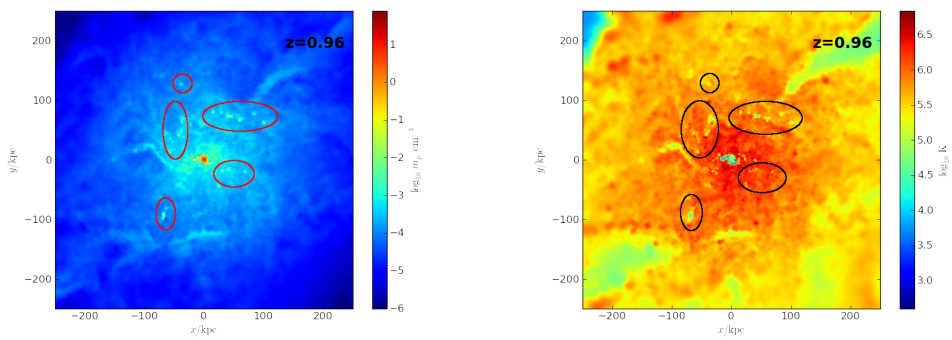

Figure 3.9: Density and temperature maps for g15784 at redshift 0.96. The cool blobs mentioned in chapter 2 have been circled for clarity.

3.5 Phase Diagrams

For each galaxy, phase diagrams were created at each output to get an idea of what the bulk of gas was doing in different parts of the galaxy. The halo was split into concentric shells of 0.2 virial radii. In each shell, a temperature-density and a radial velocity-temperature phase diagram was created. The same plots were also made for a sphere encompassing 2 virial radii. The diagrams were created as 2-D histograms, with each bin representing the total gas mass in that part of phase-space. Illustrative examples were selected and are shown in figures 3.10 - 3.13.

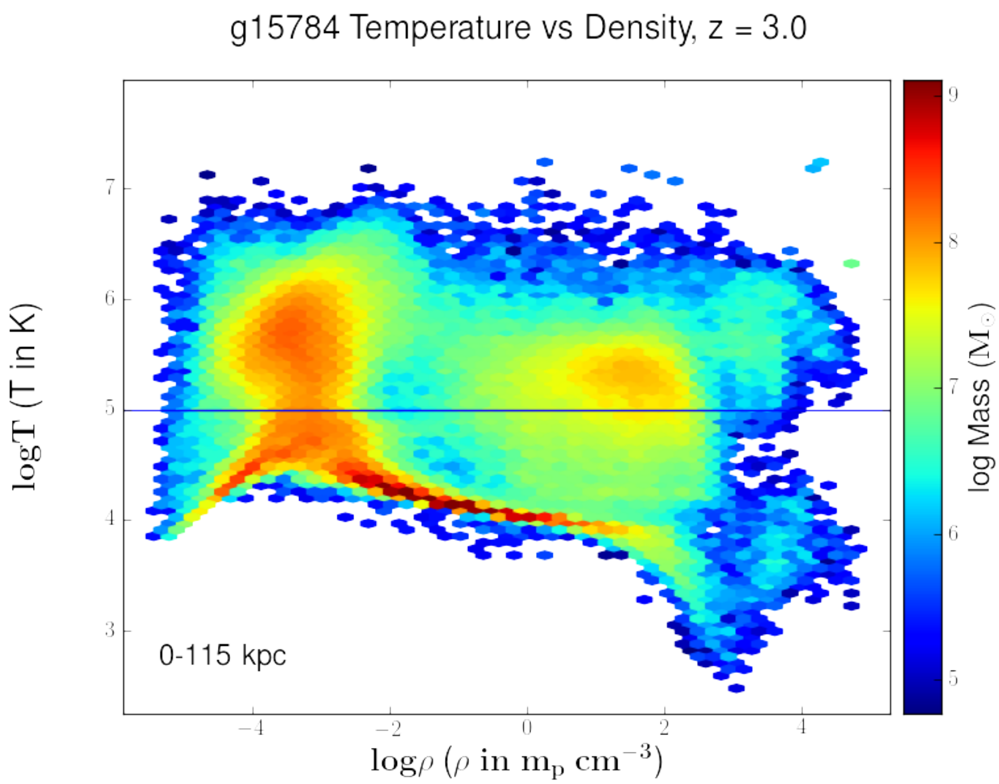

Figure 3.10: A temperature-density phase diagram for g15784 at redshift 3 across 2 virial radii. A line has been drawn in at 10^5 K to show the hot vs. cold temperature split.

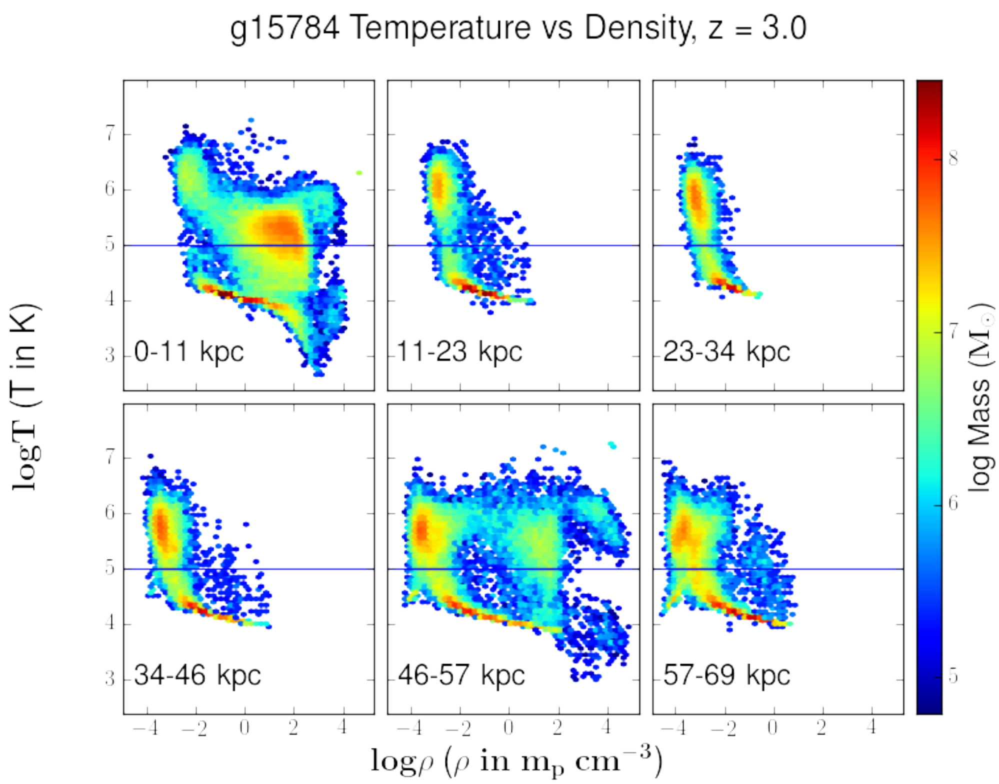

Figure 3.11: A temperature-density phase diagram for g15784 at redshift 3 in concentric shells of size 0.2 virial radii. A line has been drawn in at 10^5 K to show the hot vs. cold temperature split.

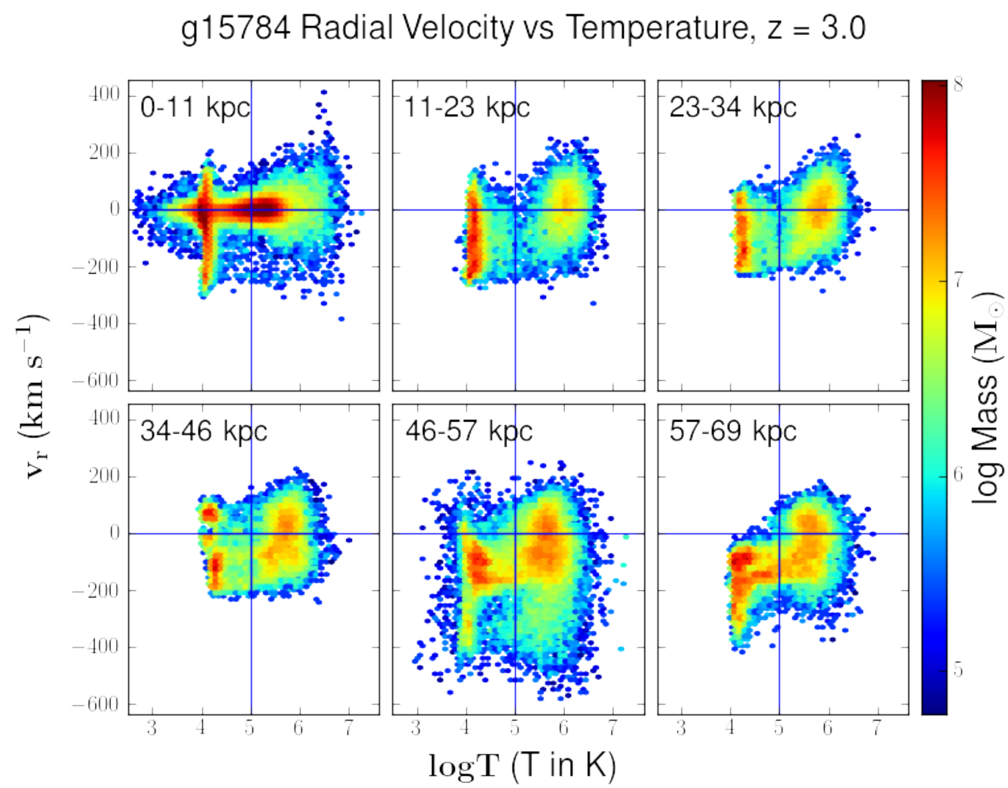

Figure 3.12: A radial velocity-temperature diagram for g15784 at redshift 3 in concentric shells of size 0.2 virial radii. A line has been drawn in at 10^5 K to show the hot vs. cold temperature split, and at 0 km/s to show which material is moving inward vs outward.

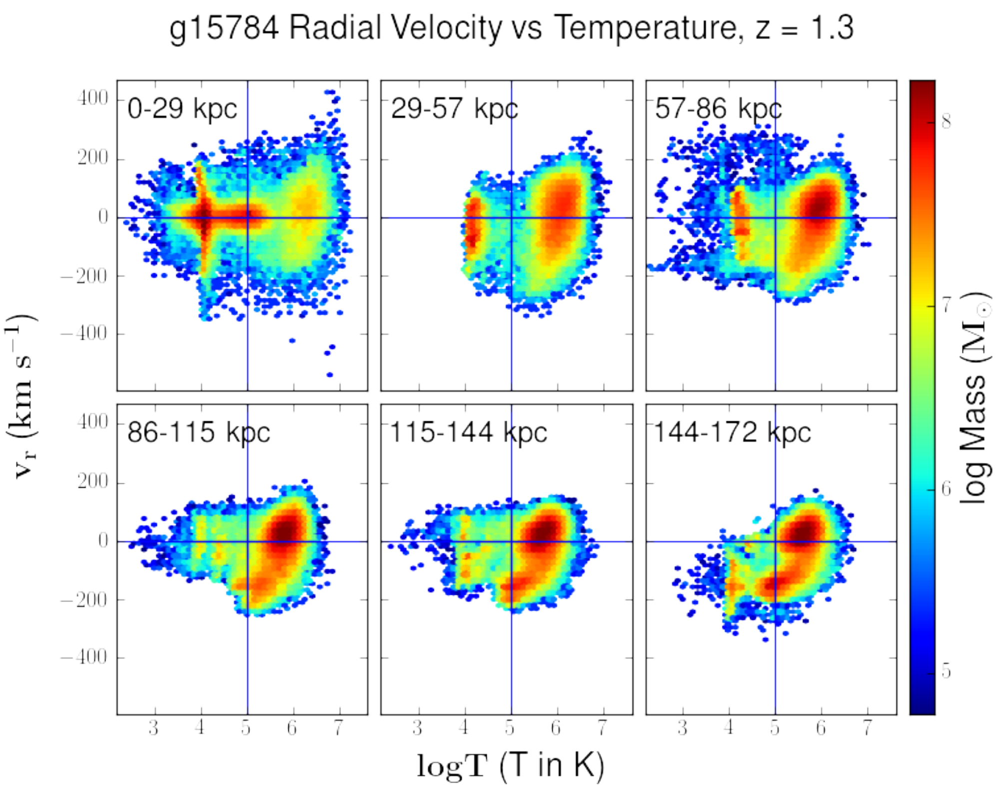

Figure 3.13: A radial velocity-temperature diagram for g15784 at redshift 1 in concentric shells of size 0.2 virial radii. A line has been drawn in at 10^5 K to show the hot vs. cold temperature split, and at 0 km/s to show which material is moving inward vs outward.

Figures 3.10 and 3.11 show a number of interesting gas properties. Figure 3.10, shows fairly clearly that a lot of gas is in the cold mode throughout the sphere, with the low densities being outside the virial radius, and the higher densities being the cold flows and disk.

In general, it's expected that the non-shocking cold flows should follow an equilibrium line in density-temperature phase space determined by adiabatic compression and cooling, and that shock heated gas should jump from about 10^4 K to somewhere between 10^5 and 10^6 K. The jump should be proportional to the infall speed, which gives a rough idea of the total mass of the halo.

Note that the density ranges used in chapter 2 (table 2.2) cover density ranges here where we can expect intense shocking.

We can then identify where each phase of gas is dominant in figure 3.11. In the inner-most bin of figure 3.11, a lot of material occupies the hot and dense part of phase space. This is likely feedback gas that has been heated by SNe and stellar winds. An important note here is that the gas doesn't quite make it to 10^6 K, the approximate virial temperature. This means the gas does not have sufficient thermal energy to escape the halo as an outflow (see e.g. Martin (2005)), and suggests that the feedback in Gasoline is either too weak, or is being dispersed over too much mass.

A thin but densely populated line in phase space at low temperature seems to be present in every shell, though it gets progressively less occupied at higher radii. The lower density part of the line represents the cold gas accreting into the galaxy and seems to be a substantial part of the gas in every shell out to about 0.6-0.8 virial radii. The high density, very low temperature (10^4 K and below) section of phase space in the first shell represents the disk, where gas is dense enough to begin cooling below 10^4 K.

Finally, the hot, low density gas in each panel represents the hot halo gas. It becomes a more substantial part of the histogram with increasing radius out to about 0.8 virial radii. It is likely that much of this is from shock heated gas. However, because the feedback gas from the disk is unable to escape, much of this hot gas may be feedback gas that has not escaped the halo. If this is the case, one can imagine a "galactic fountain" effect (e.g. Cox (1981)) where gas gets heated by feedback to sub-virial temperatures and is pushed out from the disk, eventually cooling back down to the disk of the galaxy. Note that because of the issues with feedback mentioned above, the simulations likely overestimate the amount of fountain gas.

Figures 3.12 and 3.13 show radial velocity of the gas vs temperature for redshift 3 and 1, respectively. Each shell is the same thickness, meaning that each bin is a rough proxy for mass per unit time per Kelvin, or mass flux per Kelvin. At redshift 3, it is clear that in the inner radii, cold gas dominates the inflow, falling at very high velocities. Hot gas in this region has a fairly large spread in velocity centered around 0 km/s, supporting the "galactic fountain" idea. At further radii, cold gas becomes more centered at more negative radial velocities, supporting that most of the cold gas is coming in on very radial trajectories in cold streams. Hot gas appears to stay centered on 0 km/s out to about the virial radius, supporting that it is mostly pressure supported.

By redshift 1, the cold mode accretion within the galaxy has become significantly decreased. Much more gas is in the hot mode, with a large portion of it now below the 0 km/s line. This suggests a shift of the main mode of accretion of the galaxy from cold to hot mode. Between 0.6 and 1 virial radii, there is almost no cold mode accretion. This suggest that the cold gas seen at inner radii is likely gas that has cooled from the hot halo rather than accreted from cold streams.

3.6 Star Tracking

An interesting analysis to do is to split up star formation rates of a galaxy based on how the gas accreted into the galaxy. That is, for each star particle that forms, did the parent gas particle that it formed from accrete into the galaxy via the hot or cold mode. This is a fairly tricky task and involves a number of assumptions and limits to be set. We call gas that accretes via the hot or cold mode "hot/cold mode gas", and stars that form from hot or cold mode gas "hot/cold mode stars."

The first restriction we apply is that the star had to form within 0.2 virial radii of the center of the main halo. This is a somewhat arbitrary radius to choose, however the main motivation is that we would like to exclude stars that formed in other halos and were obtained in a merger. On the other hand, many stars are formed *during* a merger, and it is very difficult to track the parent gas particle's accretion mode in these scenarios, so a radius smaller than the full virial radius should help filter these difficult particles. We call this the "r-form" criterion.

We chose to do analysis on all stars that were found within the galaxy at a redshift of 0. Since star particles in gasoline do not ever get removed, this should contain the majority of stars that were ever in the galaxy throughout the history of the simulation. Stars that were in the galaxy and ended up being stripped from the main halo are most likely stars that were temporarily in the main halo during a merger and didn't end up staying, or stars that didn't form close to the inner disk, and would be excluded by the r-form criterion.

The set of all stars that pass the r-form criterion are then binned by their formation time. The bins correspond to the times of all of the available outputs. This ensures that the formation position of each star particle is recorded at the closest output prior to formation. It is important to do so because it minimizes the distance that the halo center must be interpolated when checking the r-form criterion. Once a list of "good" stars is obtained, the parent gas particle for each star is located. If the radius of the gas particle is within 0.2 virial radii, recording of particle properties is postponed until the next output is opened. If the radius is between 0.2 and 1 virial radii, temperature, density, mass, and radial velocity are all recorded, as well as the child star properties. If the gas particle is outside of the the virial radius, the properties are recorded and the star is added to the list of "tracked" stars, meaning it will no longer be recorded at further outputs.

Finally, the recorded data is searched, starting at high redshift, for each unique gas particle. It is split into a "hot" classification based on whether its temperature was above 10^5 K at any position it was found within the virial radius. If at all points it is found to be below 10^5 K, it is classified as "cold."

In order to check the robustness of this tracking method, a second version of the tracking was performed. The difference with the second algorithm was that gas was tracked on the way in and stopped tracking once it crossed 0.2 virial radii. This avoided counting gas that was falling into the galaxy for the second time after being pushed into the halo from feedback. The way the tracking worked before, this type of gas would have been counted as hot mode accretion, even though it was only heated from feedback and not from shocking. No figures are presented from this algorithm as the difference from the first was almost undetectable.

The temperature-split gas accretion histories and star formation rates for all of the galaxies are presented in figure 3.14. A cumulative version of the same information is plotted in figure 3.16. In all figures, blue and cyan lines represent cold mode accretion and star formation while red and magenta lines represent hot mode accretion and star formation.

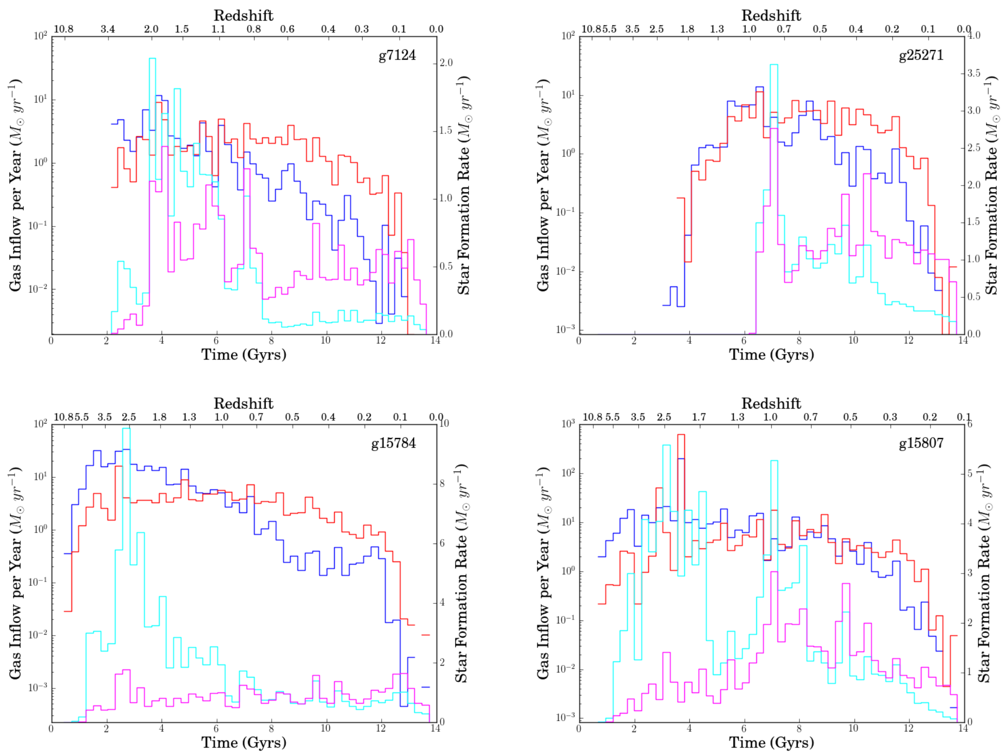

Figure 3.14: Gas accretion history for gas that turns into star particles split by accretion mode for four galaxies. A star formation history for each accretion mode is overlaid to get an idea of when the accreted gas actually forms into stars. Blue and cyan represent cold mode accretion and star formation, red and magenta represent hot mode accretion and star formation.

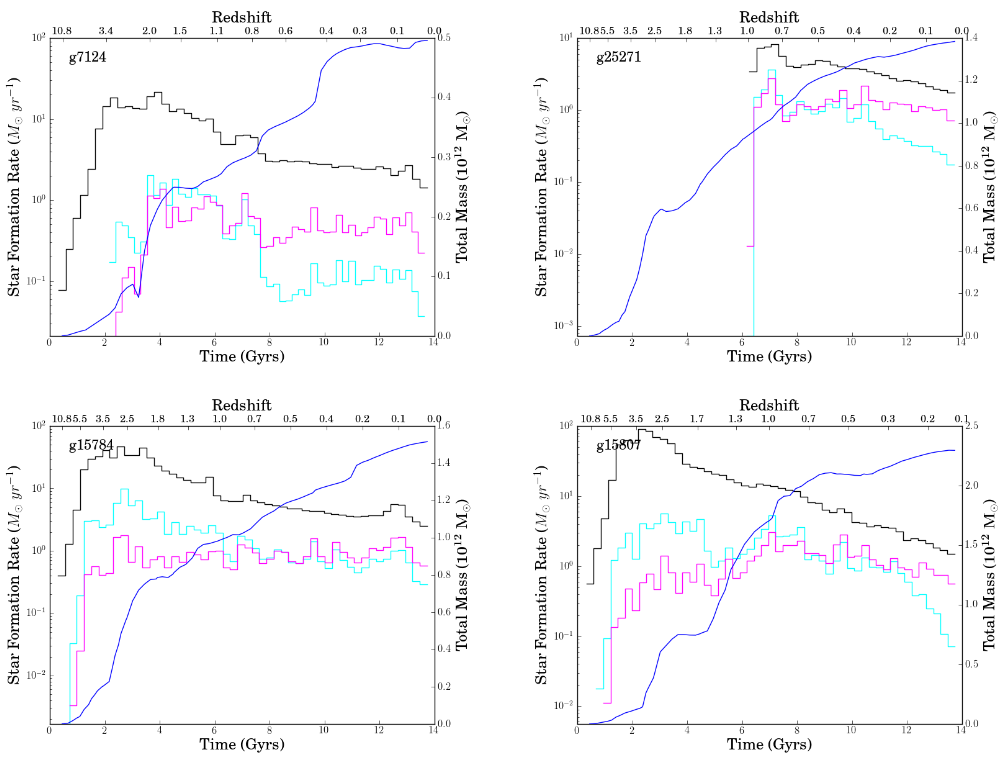

Figure 3.15: Total and temperature-split star formation rate. Cold mode star formation rate is in cyan, hot mode is in magenta, and total is in black. The blue line represents the mass history of the galaxy.

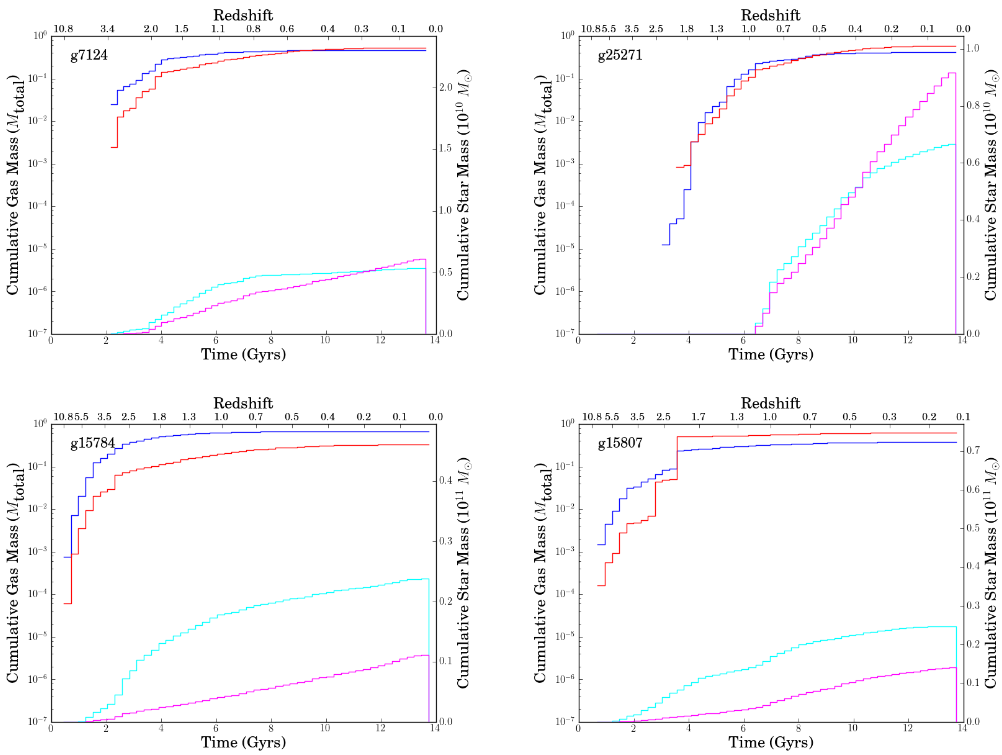

Figure 3.16: Cumulative gas accretion history for gas that turns into star particles, split by accretion mode. A cumulative star formation history for each accretion mode is overlaid to get an idea of when the accreted gas actually forms into stars and by when the majority of stars are made. Blue and cyan represent cold mode accretion and star formation, red and magenta represent hot mode accretion and star formation.

Overall, figures 3.14 and 3.16 suggest that star formation seems to be split fairly evenly between the two modes of accretion. In all galaxies, we see that cold mode accretion dominates at early times, though more strongly in the two larger galaxies. g15784 appears to be the outlier in terms of a few trends. In the three other galaxies, the amount of gas accreted by each mode is very similar, though hot mode wins out slightly. g15784, however, is quite heavily dominated by cold mode accretion, with a ratio of almost 4 to 1 by z = 0. In all cases, the total mass of stars formed from each mode is quite close, with the majority in cold mode stars for the two larger galaxies and the majority in hot mode in the two smaller galaxies.

What's particularly interesting is the pronounced difference between g15784 and g25271. Besides spin parameter, these two galaxies are *very* similar. The total mas, mass history, and redshift of last major merger are all very close, yet their temperature separated star formation is quite different. This may suggest that spin parameter is an important factor in determining hot vs cold mode accretion, as λ for g15784 is more than double that of g25271. It is unclear why this would be the case, but more investigation would be needed to clear this up. We believe this is more likely an issue of poor tracking statistics.

It is important to note however that g25271 only has half as many stars successfully tracked as g15784 (see following discussion and table 3.3), and so this may be a statistical effect. The large discrepancy in successfully tracked stars seems to largely be at the beginning of the simulation. g25271 has almost all of the stars in the first three billion years classified as "formed too far away." This may point to our r-form criterion being too strict.

It seems clear that cold gas accreted in the early universe is much more efficiently formed into stars; the star formation rate at times prior to about 8 Gyrs is heavily dominated by cold mode accretion. In the case of g7124, g25271, and g15784, it could be argued that cold mode star formation rate roughly traces cold mode gas accretion, suggesting that the gas is indeed very quickly turned into stars. g15807 also roughly follows this trend, though there is a large spike in cold mode star formation that does not have a corresponding peak in cold mode gas accretion at about 7 Gyrs. This peak does correspond to some sort of merger event, as is seen in figure 3.15. Hot mode star formation doesn't seem to have a clear trend across the four galaxies. In g15807, it roughly appears that hot mode star formation peaks about 3 Gyrs after hot mode accretion peaked, supporting the idea that hot mode accretion would have a delay of order the cooling time before forming into stars.

It is important to note that successful tracking of stars was typically quite low at about 10-20 % of the total stars in the z=0 galaxy. Table 3.3 summarizes the total number of stars that were successfully tracked in each galaxy. The "too far" column specifies the number of star particles that failed the r-form criterion. In all cases, the vast majority of stars were found to form too far from their parent galaxy, causing the low number of successfully tracked stars. This may be partly due to problems with the position interpolation described earlier in the section. However, it's likely that many of the stars simply come from merged satellites and galaxies. Accounting for this would require separately tracking gas for all merged halos as well as for the main halo. This would dramatically increase the complexity of the tracking code, and was not feasible for this project.

Table 3.3: A summary of the stars tracked for each galaxy.

Galaxy	Total Stars	Tracked Stars	Percentage	Too Far
g7124	1,160,619	181,407	15.6%	969,563
g25271	2,392,847	250,206	10.5%	2,142,525
g15784	2,594,948	553,501	21.3%	2,037,733
g15807	4,039,256	615,234	15.2%	3,420,461

Chapter 4

Conclusions

4.1 Summary

Tests of the SPH code Gasoline were performed using colliding flows of gas set up to be similar to conditions found in cosmological simulations. The colliding flows tests were run both with and without cooling and at a number of different initial densities to emulate those found in cosmological shocks. Tests were also run on a spherical adiabatic collapse of gas. Finally, a shock front from an actual cosmological simulation was examined. All of the above tests suggested that the current Gasoline viscosity parameters are not sufficient to treat shocks well at high ($M \approx 10$) Mach numbers. Significant improvement in shock treatment was attained through increasing the viscosity parameter, α, from 1 to 2 or 4. Values higher than this in α or β caused inaccurate shock solutions.

A new viscosity switch similar to that of Balsara (1995) was introduced that showed significant improvement in shock tracking. The switch showed less noise and was generally only "on" inside the shock front. However, due to the limited viscosity post-shock, solutions were more noisy and thus unacceptable.

One of the colliding flows tests demonstrated a phase separation instability in Gasoline. It was found that at specific densities and metallicities, shocking gas could separate into a cold and hot phase. This separation appeared to be seeded from the noisy shock behavior that was seen using standard viscosity values. It was suggested that this is the mechanism at play causing cold blobs to appear in the hot halos of galaxies in many numerical simulations.

Four galaxies from the MUGS project (Stinson et al., 2010) were analyzed for gas accretion behavior. Phase diagrams of the gas within 2 virial radii showed that feedback in Gasoline is insufficient to heat gas to the virial temperature, suggesting that the feedback itself is too weak or that the feedback is being distributed to too much gas. The phase diagrams also showed that cold flows were able to penetrate to between 0 and 0.2 virial radii of the galaxy center, where cold gas could be efficiently delivered to the disk.

Cold flows were found in all of the tested galaxies, which span a mass range of $5 \times 10^{11} M_{\odot}$ to $2 \times 10^{12} M_{\odot}$. Through tracking of gas particles, it was found that cold mode accretion made up a significant amount of the total gas accretion - from about 40 to 60 percent - and that most of the cold mode accretion occurred before a redshift of about 1, in agreement with the literature. The tracking was performed only for stars that formed close to the galaxy (within 0.2 virial radii), leading to a fairly small number of total star particles successfully being tracked (between 10 and 20 percent). However, out of the successfully tracked stars and gas, it was found that gas that was accreted in the cold mode was generally formed into stars much faster than hot mode gas. As well, the total mass of stars that was formed from the two modes of accretion varied significantly between the galaxies, where cold mode stars made up between 40 and 70 percent of the total mass in (tracked) stars.

4.2 Limitations, Improvements, & Future Work

As is often the case with numerical simulations, increased resolution is desired. At the current time, it is not computationally feasible to increase the resolution of our simulations by much unless we only simulate one or two galaxies. In order for the MUGS project to reach its goal of a large sample of simulated galaxies, resolution of each galaxy must be compromised. Part of the strength of this project is that analysis over multiple galaxies with different accretion histories helps to give a more general idea of the nature of cold flows. However, it may be beneficial to add a single high resolution version of a previously run galaxy, g15784 for example, in order to get increased resolution at the edge of the hot halo. As well, this run could be used to compare results with the lower resolution version in order to check convergence of properties, especially the shock behavior at the shock front, as discussed in section 2.3.4.

One of the main difficulties in the analysis of the galaxies is determining how the gas actually accreted into the galaxy. The method described in section 3.6 tried to avoid being too simplistic in determining hot vs cold accretion mode, despite this being a fairly simplistic view. In order to improve shock tracking of gas particles, a "shock" log could be added to gasoline which would record a particle and its properties any time its viscosity switch goes over some threshold value. This is an especially attractive improvement to shock tracking with the Wadsley switch, which has been shown to be *very* good at identifying shocks.

As was mentioned in section 3.6, relatively few stars were successfully tracked, likely due to the majority of stars having formed in other halos or satellites. In order to account for this, all stars that formed outside of a cutoff radius would need to be checked to see if they formed within a cutoff radius of any other bound halos. Creating a list of halos to do tracking for at each time step would leave a secondary list of halos to track stars for at the end of tracking for the first halo. This could then be repeated down to halos of a certain size. Below the size limit, gas particles could likely all be attributed to cold mode accretion since the halo would be too small to support a shock.

There are still a number of questions that remain about cold flows. While it has been shown that cold flows contribute a significant amount of fuel to galaxies, and that star formation stems equally from cold and hot mode accretion of gas, the effects of the cold flow on surrounding hot gas are not understood. An interesting idea to test would be whether cold flows actually cool surrounding hot gas into the cold flow, and/or how efficiently gas is funneled into the flow from large radii. The latter is especially of interest to try to find the impact of spin parameter on gas accretion.

In terms of the numerical aspect of this work, further testing of Gasoline in real simulations would be an excellent addition to the work presented here. Running the same IC using a few different numerical schemes, especially using the higher viscosity parameters and/or possibly an improved viscosity switch would help to give a much clearer description of the effects of viscosity on cosmological simulations.

Finally, this work has touched on the Maller-Bullock instability, suggesting that cold blobs may be forming due to noise in the gas properties. It would be very interesting to see how improved shock performance and extra physics, such as diffusion, impact the formation of these blobs. As well, work outside this thesis suggests that a different way of doing forces in SPH simulations (Ritchie & Thomas, 2001) may help diffusion of cold blobs. If numerical effects are the issue here, then a convergence study is also required.

Bibliography

Abel, T., Anninos, P., Zhang, Y., & Norman, M. L. 1997, New A, 2, 181

Agertz, O., Moore, B., Stadel, J., Potter, D., Miniati, F., Read, J., Mayer, L., Gawryszczak, A., Kravtsov, A., Nordlund, Å., Pearce, F., Quilis, V., Rudd, D., Springel, V., Stone, J., Tasker, E., Teyssier, R., Wadsley, J., & Walder, R. 2007, MNRAS, 380, 963

Avila-Reese, V., Firmani, C., & Hernández, X. 1998, ApJ, 505, 37

Balsara, D. S. 1995, Journal of Computational Physics, 121, 357

Barnes, J. & Hut, P. 1986, Nature, 324, 446

Bertschinger, E. & Jain, B. 1994, ApJ, 431, 486

Birnboim, Y. & Dekel, A. 2003, MNRAS, 345, 349

Bond, J. R., Kofman, L., & Pogosyan, D. 1996, Nature, 380, 603

Brooks, A. M., Governato, F., Quinn, T., Brook, C. B., & Wadsley, J. 2009, ApJ, 694, 396

Chapman, S. C., Smail, I., Blain, A. W., & Ivison, R. J. 2004, ApJ, 614, 671

Cole, S., Aragon-Salamanca, A., Frenk, C. S., Navarro, J. F., & Zepf, S. E. 1994, MNRAS, 271, 781

Cox, D. P. 1981, ApJ, 245, 534

Crotts, A. 1988, PASP, 100, 1331

Dekel, A. & Birnboim, Y. 2006, MNRAS, 368, 2

Dekel, A., Birnboim, Y., Engel, G., Freundlich, J., Goerdt, T., Mumcuoglu, M., Neistein, E., Pichon, C., Teyssier, R., & Zinger, E. 2009, Nature, 457, 451

Evrard, A. E. 1988, MNRAS, 235, 911

Fall, S. M. & Efstathiou, G. 1980, MNRAS, 193, 189

Faucher-Giguère, C.-A. & Kereš, D. 2011, MNRAS, 412, L118

Ferland, G. J., Korista, K. T., Verner, D. A., Ferguson, J. W., Kingdon, J. B., & Verner, E. M. 1998, PASP, 110, 761

Förster Schreiber, N. M., Genzel, R., Lehnert, M. D., Bouché, N., Verma, A., Erb, D. K., Shapley, A. E., Steidel, C. C., Davies, R., Lutz, D., Nesvadba, N., Tacconi, L. J., Eisenhauer, F., Abuter, R., Gilbert, A., Gillessen, S., & Sternberg, A. 2006, ApJ, 645, 1062

Genzel, R., Burkert, A., Bouché, N., Cresci, G., Förster Schreiber, N. M., Shapley, A., Shapiro, K., Tacconi, L. J., Buschkamp, P., Cimatti, A., Daddi, E., Davies, R., Eisenhauer, F., Erb, D. K., Genel, S., Gerhard, O., Hicks, E., Lutz, D., Naab, T., Ott, T., Rabien, S., Renzini, A., Steidel, C. C., Sternberg, A., & Lilly, S. J. 2008, ApJ, 687, 59

Genzel, R., Tacconi, L. J., Eisenhauer, F., Förster Schreiber, N. M., Cimatti, A., Daddi, E., Bouché, N., Davies, R., Lehnert, M. D., Lutz, D., Nesvadba, N., Verma, A., Abuter, R., Shapiro, K., Sternberg, A., Renzini, A., Kong, X., Arimoto, N., & Mignoli, M. 2006, Nature, 442, 786

Gingold, R. A. & Monaghan, J. J. 1977, MNRAS, 181, 375

Governato, F., Mayer, L., Wadsley, J., Gardner, J. P., Willman, B., Hayashi, E., Quinn, T., Stadel, J., & Lake, G. 2004, ApJ, 607, 688

Guedes, J., Callegari, S., Madau, P., & Mayer, L. 2011, ArXiv e-prints

Harford, A. G., Hamilton, A. J. S., & Gnedin, N. Y. 2008, MNRAS, 389, 880

Hubble, E. 1929, Proceedings of the National Academy of Science, 15, 168

Kampakoglou, M. & Silk, J. 2007, MNRAS, 380, 646

Katz, N., Quinn, T., Bertschinger, E., & Gelb, J. M. 1994, MNRAS, 270, L71+

Katz, N., Quinn, T., & Gelb, J. M. 1993, MNRAS, 265, 689

Katz, N. & White, S. D. M. 1993, ApJ, 412, 455

Kauffmann, G., White, S. D. M., & Guiderdoni, B. 1993, MNRAS, 264, 201

Kazantzidis, S., Bullock, J. S., Zentner, A. R., Kravtsov, A. V., & Moustakas, L. A. 2008, ApJ, 688, 254

Kazantzidis, S., Zentner, A. R., Kravtsov, A. V., Bullock, J. S., & Debattista, V. P. 2009, ApJ, 700, 1896

Kennicutt, Jr., R. C. 1998, ApJ, 498, 541

Kereš, D., Katz, N., Fardal, M., Davé, R., & Weinberg, D. H. 2009, MNRAS, 395, 160

Kereš, D., Katz, N., Weinberg, D. H., & Davé, R. 2005, MNRAS, 363, 2

Kimm, T., Slyz, A., Devriendt, J., & Pichon, C. 2011, MNRAS, 413, L51

Knollmann, S. R. & Knebe, A. 2009, ApJS, 182, 608

Komatsu, E., Smith, K. M., Dunkley, J., Bennett, C. L., Gold, B., Hinshaw, G., Jarosik, N., Larson, D., Nolta, M. R., Page, L., Spergel, D. N., Halpern, M., Hill, R. S., Kogut, A., Limon, M., Meyer, S. S., Odegard, N., Tucker, G. S., Weiland, J. L., Wollack, E., & Wright, E. L. 2011, ApJS, 192, 18

Kroupa, P., Tout, C. A., & Gilmore, G. 1993, MNRAS, 262, 545

Lucy, L. B. 1977, AJ, 82, 1013

Maller, A. H. & Bullock, J. S. 2004, MNRAS, 355, 694

Martin, C. L. 2005, ApJ, 621, 227

McKee, C. F. & Ostriker, J. P. 1977, ApJ, 218, 148

Mo, H. J., Mao, S., & White, S. D. M. 1998, MNRAS, 295, 319

Monaghan, J. J. 1992, ARA&A, 30, 543

Monaghan, J. J. & Lattanzio, J. C. 1985, A&A, 149, 135

Morris, J. P., M. J. J. 1997, Journal of Computational Physics, 136, 41

Nelson, R. W. & Tremaine, S. 1995, MNRAS, 275, 897

Ocvirk, P., Pichon, C., & Teyssier, R. 2008, MNRAS, 390, 1326

Peebles, P. J. E. 1969, ApJ, 155, 393

—. 1976, Ap&SS, 45, 3

—. 1978, A&A, 68, 345

Peebles, P. J. E. 1993, Principles of Physical Cosmology, ed. Peebles, P. J. E.

Perlmutter, S., Aldering, G., Goldhaber, G., Knop, R. A., Nugent, P., Castro, P. G., Deustua, S., Fabbro, S., Goobar, A., Groom, D. E., Hook, I. M., Kim, A. G., Kim, M. Y., Lee, J. C., Nunes, N. J., Pain, R., Pennypacker, C. R., Quimby, R., Lidman, C., Ellis, R. S., Irwin, M., McMahon, R. G., Ruiz-Lapuente, P., Walton, N., Schaefer, B., Boyle, B. J., Filippenko, A. V., Matheson, T., Fruchter, A. S., Panagia, N., Newberg, H. J. M., Couch, W. J., & The Supernova Cosmology Project. 1999, ApJ, 517, 565

Putman, M. E., Henning, P., Bolatto, A., Keres, D., Pisano, D. J., Rosenberg, J., Bigiel, F., Bryan, G., Calzetti, D., Carilli, C., Charlton, J., Chen, H.-W., Darling, J., Gibson, S., Gnedin, N., Gnedin, O., Heitsch, F., Hunter, D., Kannappan, S., Krumholz, M., Lazarian, A., Lasio, J., Leroy, A., Lockman, F. J., Mac Low, M., Maller, A., Meurer, G., O'Neil, K., Ostriker, J., Peek, J. E. G., Prochaska, J. X., Rand, R., Robertson, B., Schiminovich, D., Simon, J., Stanimirovic, S., Thilker, D., Thom, C., Tinker, J., Wakker, B., Weiner, B., van der Hulst, J. M., Wolfe, A., Wong, O. I., & Young, L. 2009, in Astronomy, Vol. 2010, astro2010: The Astronomy and Astrophysics Decadal Survey, 241–+

Rees, M. J. & Ostriker, J. P. 1977, MNRAS, 179, 541

Riess, A. G., Filippenko, A. V., Challis, P., Clocchiatti, A., Diercks, A., Garnavich, P. M., Gilliland, R. L., Hogan, C. J., Jha, S., Kirshner, R. P., Leibundgut, B., Phillips, M. M., Reiss, D., Schmidt, B. P., Schommer, R. A., Smith, R. C., Spyromilio, J., Stubbs, C., Suntzeff, N. B., & Tonry, J. 1998, AJ, 116, 1009

Rigby, J. R., Charlton, J. C., & Churchill, C. W. 2002, ApJ, 565, 743

Ritchie, B. W. & Thomas, P. A. 2001, MNRAS, 323, 743

Rubin, V. C., Thonnard, N., & Ford, Jr., W. K. 1978, ApJ, 225, L107

Sanchez-Saavedra, M. L., Battaner, E., & Florido, E. 1990, MNRAS, 246, 458

Seljak, U. & Zaldarriaga, M. 1996, ApJ, 469, 437

Shen, J., Abel, T., Mo, H. J., & Sheth, R. K. 2006, ApJ, 645, 783

Shen, S. 2010, PhD thesis, McMaster University

Shen, S., Wadsley, J., & Stinson, G. 2010, MNRAS, 407, 1581

Silk, J. 1977, ApJ, 211, 638

Somerville, R. S. & Primack, J. R. 1999, MNRAS, 310, 1087

Spergel, D. N., Bean, R., Doré, O., Nolta, M. R., Bennett, C. L., Dunkley, J., Hinshaw, G., Jarosik, N., Komatsu, E., Page, L., Peiris, H. V., Verde, L., Halpern, M., Hill, R. S., Kogut, A., Limon, M., Meyer, S. S., Odegard, N., Tucker, G. S., Weiland, J. L., Wollack, E., & Wright, E. L. 2007, ApJS, 170, 377

Springel, V. 2010, ARA&A, 48, 391

Springel, V., Yoshida, N., & White, S. D. M. 2001, New A, 6, 79

Stadel, J. G. 2001, PhD thesis, UNIVERSITY OF WASHINGTON

Stark, D. P., Swinbank, A. M., Ellis, R. S., Dye, S., Smail, I. R., & Richard, J. 2008, Nature, 455, 775

Steidel, C. C., Erb, D. K., Shapley, A. E., Pettini, M., Reddy, N., Bogosavljević, M., Rudie, G. C., & Rakic, O. 2010, ApJ, 717, 289

Steinmetz, M. & Mueller, E. 1993, A&A, 268, 391

Stewart, K. R., Kaufmann, T., Bullock, J. S., Barton, E. J., Maller, A. H., Diemand, J., & Wadsley, J. 2011, The Astrophysical Journal Letters, 735, L1

Stewart, K. R., Kaufmann, T., Bullock, J. S., Barton, E. J., Maller, A. H., Diemand, J., & Wadsley, J. 2011, ApJ, 738, 39

Stinson, G., Seth, A., Katz, N., Wadsley, J., Governato, F., & Quinn, T. 2006, MNRAS, 373, 1074

Stinson, G. S., Bailin, J., Couchman, H., Wadsley, J., Shen, S., Nickerson, S., Brook, C., & Quinn, T. 2010, MNRAS, 408, 812

Stringer, M. J. & Benson, A. J. 2007, MNRAS, 382, 641

Toth, G. & Ostriker, J. P. 1992, ApJ, 389, 5

Tsuchiya, T. 2003, Ap&SS, 284, 515

Velazquez, H. & White, S. D. M. 1999, MNRAS, 304, 254

Velazquez, H. M. 2001, in Revista Mexicana de Astronomia y Astrofisica Conference Series, Vol. 11, Revista Mexicana de Astronomia y Astrofisica Conference Series, 189–+

Wadsley, J. W., Stadel, J., & Quinn, T. 2004, New A, 9, 137

Wadsley, J. W., Veeravalli, G., & Couchman, H. M. P. 2008, MNRAS, 387, 427

White, S. D. M. & Frenk, C. S. 1991, ApJ, 379, 52

Williams, L. L. R., Navarro, J. F., & Bartelmann, M. 1999, ApJ, 527, 535

Zel'Dovich, Y. B. 1970, A&A, 5, 84

Zwicky, F. 1937, ApJ, 86, 217

This page intentionally left blank.